Microstructures, hydrogen concentrations, and seismic properties of a tectonically exhumed sliver of oceanic mantle lithosphere, Moa Island, Timor-Tanimbar outer-arc, eastern Indonesia

Sylvie Demouchy, Fabrice Barou, Akira Ishikawa, Emmanuel Gardés, Andrea Tommasi

Tectonophysics 887 (2024) 230443

Contents lists available at ScienceDirect

Tectonophysics

journal homepage: www.elsevier.com/locate/tecto

Microstructures, hydrogen concentrations, and seismic properties of a tectonically exhumed sliver of oceanic mantle lithosphere, Moa Island, Timor-Tanimbar outer-arc, eastern Indonesia

Sylvie Demouchy [a,*], Fabrice Barou [b], Akira Ishikawa [c,d], Emmanuel Gardés [a], Andréa Tommasi [b]

[a] Laboratoire Magmas et Volcans, Université Clermont Auvergne, CNRS, IRD & OPGC, UMR 6524, F-63170 Aubière, France
[b] Geosciences Montpellier, CNRS & Université de Montpellier, Montpellier 34095, France
[c] Department of Earth and Planetary Sciences, Tokyo Institute of Technology, 2-12-1 Ookayama, Meguro-ku, Tokyo 152–8550, Japan
[d] Research Institute for Marine Resources Utilization, Japan Agency for Marine-Earth Science and Technology, 2–15, Natsushima, Yokosuka, Kanagawa 237–0061, Japan

ARTICLE INFO

Keywords:
Earth mantle
Oceanic mantle lithosphere
CPO
Melt percolation
Hydrogen
NAMs
Seismic anisotropy

ABSTRACT

We characterize and quantify the microstructure, hydrogen concentrations, and seismic properties of a tectonically exhumed sliver of oceanic lithospheric mantle outcropping in the Moa Island (Leti archipelago, Timor-Tanimbar outer-arc). The 18 spinel peridotites (lherzolites and harzburgites) have coarse-porphyroclastic microstructures and olivine crystal-preferred orientations (CPO) with axial-[010] (also known as AG-type) or [100](010) (A-type) patterns, similar to those observed in peridotitic xenoliths from oceanic mantle lithosphere. These coarse-porphyroclastic microstructures are variably overprinted by growth of strain-free olivine neoblasts and crystallization of secondary pyroxenes. Recrystallized fractions vary from 6.9 up to 31.3%. The interstitial (cuspate) shapes and CPOs of clinopyroxene, uncorrelated with the olivine CPOs, indicate that refertilization by a reactive melt percolation post-dated deformation. Seismic properties are calculated based on the modal compositions and CPOs of all samples. Increase in the recrystallized olivine fraction decreased the seismic anisotropy, since static recrystallization produced some dispersion of the CPO, but did not change drastically the texture acquired during deformation. Mean seismic velocities (mean Vp = 7.9 km.s^{-1}; mean Vs = 4.5 km.s^{-1}) and anisotropy (mean maximum S wave polarization anisotropy = 4.5%), estimated by considering coherent orientation of the foliation and lineation of all samples, are within the range of typical values for the uppermost mantle. The nominally anhydrous minerals contain small amounts of hydrogen (olivine: 13–18 ppm H_2O by weight; orthopyroxene: 58–175 wt ppm H_2O and clinopyroxenes: 244–288 wt ppm H_2O). A bulk water content of 50 wt ppm H_2O is estimated based on nomminally anhydrous minerals for the Moa peridotites, in agreement with previous estimates for the oceanic mantle lithosphere based on peridotitic xenoliths. This is the first direct measurement of hydrogen concentrations in peridotites from an oceanic mantle lithosphere which experienced melt extraction.

1. Introduction

The current database for microstructures, crystal preferred orientations, and hydrogen concentrations in mantle peridotites is still limited when the diversity of geological settings is considered or when compared to other databases such as the one for Rare Earth Element in mantle specimens (e.g., Demouchy and Bolfan-Casanova, 2016; Demouchy and Alard, 2021). One type of mantle specimens is particularly overlooked when estimating volatiles contents: tectonically exhumed peridotite massifs (cf. the review by Bodinier and Godard, 2014), such as orogenic massifs (e.g., Ronda, Beni-Boussera, Lanzo), ophiolitic outcrops (e.g., Oman, Troodos, Josephine), mantle slivers exhumed due to local compression during oceanic ridge centers (Zabargad in the Red Sea; St. Paul and the Vema fracture zone in the Atlantic Ocean, Le Roux et al., 2021), or roots of island arcs (e.g., Sapat, Talkeetna). Some of the primary reasons are that outcrops of mantle

* Corresponding author.
E-mail address: sylvie.demouchy@uca.fr (S. Demouchy).

https://doi.org/10.1016/j.tecto.2024.230443
Received 24 March 2024; Received in revised form 30 July 2024; Accepted 31 July 2024
Available online 3 August 2024

rocks both of continental or oceanic provenance are rare. They are also frequently extensively serpentinized, leading to recurrent overestimates of hydrogen concentration in mantle minerals. Reliable data on hydrogen concentrations in minerals of mantle peridotite massifs representative of the continental lithosphere remain scarce (e.g., Kim and Jung, 2015). Furthermore, late tectonic events associated or not with melt or fluids rock interactions can develop in the mantle lithosphere, even prior to the tectonic exhumation (e.g., Le Roux et al., 2007). Such events can perturbate the initial hydration state of a peridotite.

Here, we investigate a new outcrop of tectonically exhumed peridotites, located in the non-volcanic outer-arc of Timor-Tanimbar region (eastern Indonesia, Fig. 1), the Moa Island. The first objective is to improve the representativity of both the microstructural and hydrogen databases for oceanic mantle lithosphere, which up to now relies essentially on observations on peridotitic xenoliths (e.g., Peslier, 2010; Bernard et al., 2019; Demouchy and Bolfan-Casanova, 2016). Mantle xenoliths from arc islands are notoriously rare due to the reactivity with arc magmas (boninites, andesites), which has led to a quasi-absence in the current database of H concentrations (only three localities: Kamtchatka, Ichinomegata and Oki-dogo (Japan arc) (e.g., Soustelle et al., 2010; Demouchy et al., 2015; Satsukawa et al., 2017). Likewise, mantle xenoliths from oceanic settings far from plate boundaries are limited, with studies on Hawaii (Peslier et al., 2015; Demouchy and Alard, 2021) or Ontong-Java Plateau (Demouchy et al., 2015). The second objective is to try to pinpoint the link between melting, reactive melt transport, hydrogen concentrations, ductile deformation, and potential impact on the seismic properties. To fulfill these objectives, we performed microstructural analyses and measured hydrogen concentrations of a series of samples from the very fresh peridotite massif in the Moa Island (Fig. 1).

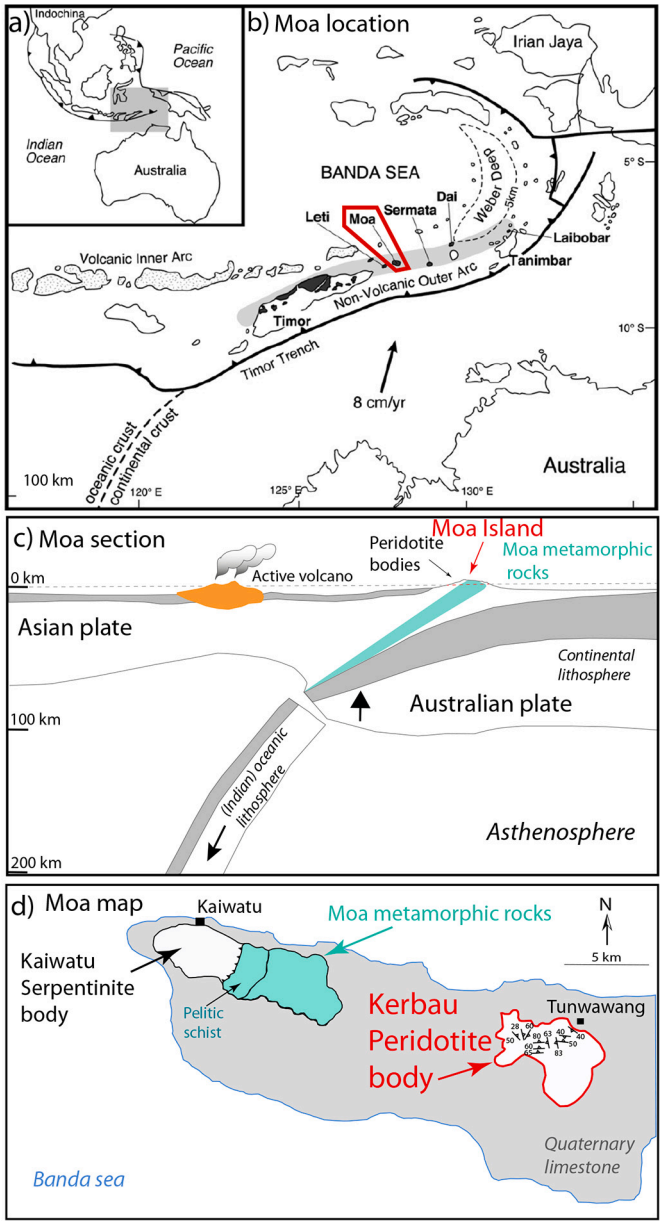

Fig. 1. (a) Location of the Leti Island archipelago along the Indonesian arc; (b) location of the Moa Island within Leti Island archipelago in the non-volcanic outer-arc of Timor-Tanimbar region; Note that the island cluster Leti-Moa-Lakor is commonly referred as Leti Islands (e.g., Courdurier-Curveur et al., 2021). (c) Section across Moa Island showing the partial slab break-off and the metamorphic rock belt within the Moa Island; d) Simplified geological map of Moa Island with the setting of the two mantle outcrops: West, the serpentinized peridotite massif Kaiwatu, and East the fresh peridotite massif of Kerbau, (redrawn from Kaneko et al., 2007).

2. Materials and methods

2.1. Geological context and studied samples

The Moa Island is part of the Leti archipelago, which is a segment of the non-volcanic outer-arc of Timor-Tanimbar. This non-volcanic arc is located in front of the current active fore-arc basin. This outer-arc formed by doming of the oceanic plate in response to the subduction and partial break-off of the Indo-Australian slab (Fig. 1c) beneath the over-riding Asian plate. The several islands of the Leti archipelago expose one of the youngest (late Miocene) metamorphic belts in the world (e.g., Kaneko et al., 2007; Kadarusman et al., 2010). This metamorphic belt is associated with peridotite slivers, among which the one studied here, which were not – a priori – modified by late tectonic events. Moa is a small island (30 km × 10 km, Fig. 1d) composed of three tectonostratigraphic sequences (Fig. 1d): (1) the metamorphic belt, (2) the relics of an oceanic plate, represented by both serpentinized and fresh peridotites bodies, and (3) the quaternary reef limestone.

The peridotites occur in two isolated massifs (Fig. 1d): Kaiwatu (West) and Kerbau (Est). The Kerbau massif (375 m of altitude) is composed of exceptionally fresh spinel-bearing peridotites, mostly lherzolites, with very minor serpentinization, whereas the Kaiwatu peridotites are almost fully serpentinized (Ishikawa et al., 2021). Both peridotite bodies are interpreted as a section of the (over-riding) oceanic Asian plate exhumed by doming in response to collision with Australian plate. This exhumation was probably favored by the partial break-off of the Indo-Australian slab (Kaneko et al., 2007; Ishikawa et al., 2007).

The present study focuses on 18 samples of peridotites (harzburgite and lherzolites) from the Kerbau massif. Previous petrochemical studies have inferred that the harzburgites are residual peridotites, resulting from a continuous melt extraction, similar to what is happening with decompression melting at an oceanic ridge center (Ishikawa et al., 2007). However, the Moa peridotites were equilibrated at too shallow depths to represent the mantle source of the early-stage boninitic magmas (high-Mg andesites), which outcrop as ~10 Ma gabbro-norite intrusions in the adjacent Kaiwatu massif (Ishikawa et al., 2007, their Fig. 13; Lin et al., 2023).

At the macroscale, the Kerbau peridotites studied here are exceptionally fresh and display a foliation defined by elongated olivine porphyroclasts enclosed in a fine-grained olivine-rich matrix. They are suitable for Fourier transform infrared spectroscopy (FTIR) and electron backscatter diffraction (EBSD) analyses, and potentially fresh enough to investigate the presence of remnant melt at triple junctions or along grain boundaries. Equilibrium temperatures were obtained using two geothermometers (Brey and Köhler, 1990; Putirka, 2008), based on the equilibrium between ortho- and clinopyroxene major and trace-element

concentrations. Since there are no reliable geobarometers for spinel-peridotites, we assumed an equilibrium pressure of $P = 1.2$ GPa (~ 42 km of depth), and an equilibrium temperature of 900 ± 50 °C (Table 1, and Supplementary Material Fig. S1).

2.2. Sample preparation

The microstructures of the Moa peridotites were first studied by optical microscopy on petrographic thin sections (30 μm) and then by high resolution scanning electron microscopy (SEM). A first set of thin sections was cut in random orientations due to the small sizes of the available samples, and then embedded in epoxy, polished with diamond pastes (down to 0.25 μm), followed by a final chemo-mechanical polish with colloidal silica (0.04 μm particles for at least 1 h) for EBSD analyses. For FTIR, a second set of thick sections was also cut in random orientations relative to the foliation or lineation of the peridotites, and double side polished by hand with diamond pastes (down to 0.1 μm) to final a thickness between 462 and 633 μm. The thickness of each section is reported in Table S1.

2.3. Scanning electron microscopy

To investigate the potential presence of hydrous minerals along grain boundaries or fractures or the presence of remanent melt, petrographic thin sections of Moa13, which is the most recrystallized, and Moa37, the least recrystallized sample, were imaged by SEM and HR-SEM. The sections are prepared for SEM investigation with deposition of a ~ 20 nm carbon layer after the EBSD analyses. Backscattered electron images were acquired at 10 kV and 0.8 nA using the SEM ThermoFisher® Helios 5 PFIB CXe at Laboratoire Magmas et Volcans (France). For identification of phases with sizes below 10 μm, which could not be achieved by EBSD mapping, energy dispersive spectroscopy (EDS) maps were acquired at 10 kV and 3.2 nA using the Esprit software from Brucker™.

2.4. Electron backscattered diffraction

The microstructural data, including crystal preferred orientations (CPO), were determined by indexation of electron-backscattered diffraction patterns (EBSD) in automatic mapping mode in a SEM CamScan X500FE CrystalProbe at low vacuum at Geosciences Montpellier (France). The working distance was 25 mm, acceleration voltage 20 kV, and the beam current 10 nA for EBSD mapping and 5 nA for backscattered electron imaging (BSE). No carbon coating is applied on the surface of the thin section prior to EBSD analyses, but the thin section is surrounded by copper-carbon tape. We analyzed crystal orientations of olivine, diopside, enstatite, spinel (chromite), phlogopite and pargasite, using the Aztec software from Oxford Instruments HKL. The analyzed area covers at least 1/2 of each thin section with various step sizes: 3 μm for samples Moa3, Moa4 and Moa5 (detailed maps) and 10 μm for the 15 other samples (from Moa7 to Moa56, see Table 1). Indexation rates in the raw maps range from 90.6 to 98.4%.

Post-acquisition data treatment consisted of (i) filling the non-indexed pixels which have up to 8 identical neighbors with the same orientation, (ii) repeating this operation using respectively 7, and 6 identical neighbors, (iii) identifying the grains, i.e., continuous domains characterized by an internal misorientation <15°, and (iv) within each olivine crystal, searching and correcting for rare systematic indexation errors due to the olivine hexagonal pseudo-symmetry, which results in similar diffraction patterns for orientations differing by a rotation of 60° around [100]. At each step, the resulting orientation maps are checked to avoid over-extrapolation of the data (e.g., artificial increase of grain size). The EBSD maps for all samples are provided in Fig. S2.

Crystal preferred orientation maps were further treated with the MTEX toolbox in Matlab (Hielscher and Schaeben, 2008; Bachmann et al., 2010). The orientation distribution function (ODF) describing the CPO is calculated using a de la Vallee Poussin kernel with axial-symmetry), with half-width of 10° (bandwidth of 28 in spherical harmonic coefficients). The intensity of the CPO is characterized by the texture J-index computed as the integral of the square of the ODF (Bunge, 1982). We used the BA-, BC-, and AC-indexes to quantify the symmetry of olivine CPO. These three indexes, which are estimated from the eigenvalues of the distributions of the [100], [010], [001] axes, (also called a, b, and c), describe the symmetry of the CPO (Mainprice et al., 2014). The BA-index allows classifying the olivine CPO into three categories: (i) fiber-[010], characterized by a [010] point maximum and girdle distributions of [100] and [001] (BA-index <0.35), (ii) orthorhombic (dominant slip system [100](010)), characterized by point maxima of all [100], [010] and [001] (0.35 < BA-index <0.65), and (iii) fiber-[100], characterized by a point maximum of [100] and girdle distributions of [010] and [001] (BA-index >0.65). Similarly, BC- or AC-indexes are used to discriminate between point and girdle distributions of [010] and [001], or [100] and [001], respectively.

CPO of olivine, orthopyroxene (Opx), and clinopyroxene (Cpx) are displayed as pole figures. Orientation densities in the pole figures are

Table 1
Summary of the key petrological indicators of the studied coarse-porphyroclastic Moa peridotites. Amount of recrystallized olivine, volume fraction of each major phase, Olivine Fo# defines as Fo# = 100 × (Mg/Mg + Fe), and two-pyroxenes equilibrium temperatures determined using P: Putirka (2008) and BKN: Brey and Köhler (1990). Equilibrium temperatures with error bars are displayed in Fig. S1. Volume fraction of phlogopite and pargasite are both well below 0.1% even if trace amount were found in SEM in the peridotites from Moa Island.

	Lithology	Ol Rex %	Ol %	Opx %	Cpx %	Sp %	Fo in Ol	T°C eq. P	T°C eq. BKN
Moa3	Harzburgite	13.2	86.4	8.6	4.9	0.1	90.88	1010	950
Moa4	Lherzolite	31.3	59.3	30.1	8.7	1.9	91.27	970	860
Moa5	Lherzolite	12.9	62.1	27.9	9.3	0.7	91.10	950	850
Moa7	Harzburgite	9.5	77.0	17.4	4.8	0.7	90.75	940	830
Moa10	Lherzolite	9.6	65.8	26.5	7.3	0.4	n.d.	n.d.	n.d.
Moa12	Lherzolite	20.3	66.2	26.9	6.4	0.4	n.d.	n.d.	n.d.
Moa13	Lherzolite	29.0	69.5	23.4	5.4	1.8	n.d.	n.d.	n.d.
Moa16	Lherzolite	22.6	63.1	24.3	12.1	0.4	n.d.	n.d.	n.d.
Moa20	Lherzolite	12.6	70.2	21.0	6.9	1.8	n.d.	n.d.	n.d.
Moa22	Lherzolite	10.8	76.6	16.9	5.9	0.6	n.d.	n.d.	n.d.
Moa24	Harzburgite	28.4	64.6	32.4	2.5	0.6	n.d.	n.d.	n.d.
Moa30	Lherzolite	15.9	69.3	24.4	5.3	1.0	90.82	940	860
Moa31	Harzburgite	18.3	75.7	20.1	3.0	1.3	n.d.	n.d.	n.d.
Moa34	Harzburgite	9.6	69.1	27.3	3.0	0.6	n.d.	n.d.	n.d.
Moa37	Lherzolite	12.6	65.5	25.2	7.9	1.4	90.63	950	830
Moa50	Harzburgite	6.9	79.0	17.8	2.8	0.3	90.97	950	850
Moa55	Lherzolite	17.6	66.2	26.6	5.7	1.5	n.d.	n.d.	n.d.
Moa56	Lherzolite	14.7	69.6	22.2	7.5	0.6	n.d.	n.d.	n.d.

normalized to a uniform distribution (multiple uniform density: MUD). Since the thin sections are cut in random orientations relative to the lineation and the foliation, to allow for easy comparison between the CPO of different samples, the CPO data for all minerals are then rotated as to have the maximum concentration of the olivine [100] axes in the East or West direction of the pole figure and the maximum concentration of [010] axes close to the North or South. This procedure is rather classic for displaying CPO data of mantle xenoliths (e.g., Demouchy et al., 2019; Tommasi et al., 2020). It is justified here by the analysis of (i) the relative intensity of the orientation of [100], [010], and [001] axes of olivine, (ii) the relations between olivine and pyroxene CPOs, and (iii) the relations between olivine CPO and shape-preferred orientation (SPO), when the latter could be observed in thin sections. It implies that for olivine deformed dominantly by [100](010) slip system, the olivine [100] maximum defines the orientation of the flow direction (lineation, oriented *E*-W in the pole figures) and the [010], the orientation of the normal to the flow plane (foliation, the normal axis is N-S in the pole figures), an assumption justified a posteriori by the observations (section 5).

We used the Bachmann et al. (2010) grain detection method in MTEX with a misorientation threshold of 15° to identify the grains. Grains composed by <10 pixels are not considered in the analysis of grain sizes and shapes. Grain sizes are two dimensional (2D) equivalent diameter values estimated as the diameter of a circle with the same area as the grain. There are apparent grain sizes, not corrected for sectioning effect. Samples are characterized by both the arithmetic mean of the grain size and the area-weighted mean grain size. Aspect ratios are in most cases underestimated, since they are 2D measurements in sections with variable orientations relatively to the deformation reference frame. We choose to use area weighted values for characterizing the grain size and aspect ratio of olivine and pyroxenes in the different samples, since (1) they give closer values to the visual estimate when observing the thin section than the arithmetic means and (2) to maintain consistency with seismic properties, which depend on mineral mode (mineral fractions) and not on the number of grains along the wave path. We characterize the sinuosity of the grain boundaries by the shape factor, which is the perimeter of the grain divided by the perimeter of a circle with identical area. The misorientation angle of each pixel relative to the mean orientation of the grain (Mis2Mean) and the grain orientation spread (GOS), which is the standard deviation of the orientations within a grain, are calculated to quantify the intragranular disorientation gradients. Both are proxies of the density of geometrically necessary dislocations within the grain (see Demouchy et al., 2023). Both the intragranular misorientation and the sinuosity of grain boundaries should decrease in response to recrystallization. Following Tommasi et al. (2020), we used EBSD orientation maps to estimate the recrystallized (newformed) fraction (Rex %) of olivine (Table 1, Fig. S2), which is defined as the area fraction of olivine grains with both (i) a grain size smaller than10 times the mean grain size μm (~500 μm in most samples) and (ii) a grain orientation spread (GOS) smaller than 1.5°. Both criteria are defined arbitrary, but have proven to effectively discriminate between parent and recrystallized grains in previous microstructural studies of peridotites (e.g., Tommasi et al., 2020; Lopez-Sanchez et al., 2021).

2.5. Seismic properties

Seismic properties of all samples were calculated using the CPO of olivine, Opx, and Cpx, and their respective mode estimated from EBSD phase maps (Mainprice, 1990). The elastic constants of olivine, Opx, Cpx, and their pressure and temperature derivatives are from Abramson et al. (1997), Chai et al. (1997a, 1997b), and Sang and Bass (2014), respectively. The elastic constant tensors are calculated for a temperature of 900 °C, which is the mean equilibrium temperature of the Kerbau peridotites (Table 1, Fig. S1), and an arbitrary pressure of 1.2 GPa (~ 42 km of depth, constrained by the absence of garnet and plagioclase). The seismic properties are calculated using a Voigt–Reuss–Hill mean. We present the seismic properties of three representative samples (Moa13, Moa30 and Moa50) as well as mean seismic properties calculated by averaging the elastic constant tensors of all 18 spinel peridotite samples rotated into a common structural reference frame. These mean seismic properties thus consider a geographically coherent orientation of the foliation and lineation for all samples. Consequently, they represent an upper-bound estimate of the seismic anisotropy of the Moa peridotites at the km-scale.

2.6. Fourier transform infrared spectroscopy

Fourier transform infrared spectroscopy (FTIR) is used to qualify hydrogen speciation and to quantify hydrogen concentration in transmission mode using a Bruker Vertex 70 spectrometer at the Laboratoire Magmas et Volcans (France). The IR spectrometer is coupled to a Bruker HYPERION microscope equipped with a liquid nitrogen cooled MCT detector (Mercatel alloy, HgCdTe), a mid-infrared light (Globar™) and a KBr/Ge beam splitter. The wavenumber has a resolution of ±2 cm^{-1}. We used square (100 × 100 μm or 50 × 50 μm) or rectangular apertures (100 × 50 μm) to best match optically clear, free-cracks or inclusion-free areas. Since the measurements are performed on a rock section with grains of variable crystallographic orientations relative to the IR beam, we used exclusively unpolarized infrared spectra, following the protocol of Denis et al. (2015). Each IR spectrum was normalized to 1 cm of thickness, and corrected for baseline first using the OPUS software. When needed, spectrum are further corrected using the spline function using Igor Pro™.

Two different types of infrared calibrations are used to calculate H concentrations: (i) the empirical frequency-dependent the calibration of Paterson (1982) for unpolarized infrared spectra for olivine, Opx and Cpx, and (ii) two mineral-dependent calibrations, the calibration of Bell et al. (1995) for pyroxenes and the calibration of Withers et al. (2012) for olivine. These calibrations result in a detection limit of about 1 ppm wt H_2O for a 1-mm-thick olivine sample (Denis et al., 2015). The estimated error from the empirical calibration in the resulting H concentration in olivine is around 30% for the calibration of Paterson (1982). It is lower, around 20% for the calibration of Bell et al. (1995) and around 15% for the calibration of Withers et al. (2012). To apply the frequency-dependent calibration of Paterson (1982), we used the following mineral specific factors χ_i (cf. Paterson, 1982; Demouchy and Bolfan-Casanova, 2016): χ_{ol} = 2695 wt ppm H_2O for Fo_{90}, χ_{Opx} = 2727 wt ppm H_2O for Opx, and χ_{Cpx} = 2769 wt ppm H_2O for Cpx; ζ, the orientation factor, equals 1/3 for unpolarized infrared analyses on unoriented grains (Paterson, 1982). The spectrum was integrated between 3600 and 3100 cm^{-1} for olivine, 3610 and 3000 cm^{-1} for Opx, and between 3670 and 3000 cm^{-1} for Cpx. To apply the calibration of Withers et al. (2012), we multiply the mean spectra obtained by unpolarized infrared by a factor of three as it yields estimates comparable to the total absorption coefficient obtained from polarized infrared spectra along the three main crystallographic axes (see suppl. Fig. S1 in Férot and Bolfan-Casanova, 2012). Ideally, at least 10 spectra per grain with different orientations relative to the IR beam should be acquired and averaged to improve accuracy of the measurements (Kovàcs et al., 2012). Unfortunately, we could not always apply this recommendation during this study. The individual absorption coefficients are reported in Table 3 and Table S1, allowing for re-calculation of concentrations using past or future IR calibrations. This also allows comparison with previous data using the calibration of Bell et al. (2003) for olivine. This latter calibration is not used here since it overestimates hydrogen concentrations in olivine (see Withers et al., 2012 for details).

A recurrent challenge for hydrogen quantification in nominally anhydrous minerals (NAM) in peridotite from massifs is the pervasive contamination by hydrous minerals formed during low-temperature processes (mostly serpentine, identifiable by FTIR as a OH band at 3680–3690 cm^{-1}, see Post and Borer, 2000, Jung et al., 2013, 2014; Park and Jung, 2017). This contamination leads most often to

overestimate the hydrogen concentration in olivine. Attempts were made to quantify hydrogen in NAMs using other methods such as secondary ion mass spectrometry, but this technique does not permit to identify and then exclude contamination by hydrous minerals from alteration, also leading to questionable water contents in olivine (e.g., Skemer et al., 2013).

3. Results

3.1. Mineralogy

The main petrological and mineralogical features of the studied samples are compiled in Table 1. Based on the mineral modes obtained by EBSD (Cpx fraction ranging from 2.5% to 12.5%), among the 18 studied samples, six are spinel-bearing harzburgites (Moa3, Moa7, Moa24, Moa31, Moa34 and Moa50) and the others are spinel-bearing lherzolites. We recall that constituent mineral analyses indicated a very homogeneous forsterite content (defined as Fo =100 x Mg/(Mg + Fe)) ranging between 90.6 and 91.8. Alumina contents in orthopyroxenes range between 1.8 and 3.9 Al_2O_3 wt%, and spinel has Cr# (defined as Cr# = 100 x Cr/(Cr + Al + Fe^{3+}) ranging from 0.24 to 0.46 (see Ishikawa et al., 2007, for the original set of chemical compositions).

3.2. Microstructures

All studied peridotites have a partially recrystallized coarse-porphyroclastic microstructure with local enrichment in pyroxenes, often forming vein-like domains or diffuse layering (cf. Moa3, Moa13 Moa16, Moa30, Moa31). Yet the intensity of recrystallization, defined as the area fraction of olivine neoblasts relative to the total olivine area in EBSD maps, varies from 6.9% up to 31.3% (Table 1). This microstructure is illustrated in Figs. 2 and 3 (see Fig. S2 for the full data set). The olivine porphyroclasts display well developed undulose extinction, subgrain boundaries and often surrounded by small new formed (neoblasts) olivine grains (e.g., Moa3, Fig. S2). The olivine neoblasts, grains formed by recrystallization, are either dispersed or form discontinuous layers parallel to the porphyroclasts elongation direction. Statistics for key microstructural parameters of olivine are provided in Table 2 (see Table S2 for the full data set). The mean area-weighted olivine grain size ranges from 46 to 103 μm; the mean area-weighted olivine shape factor (a proxy for tortuosity of grain boundaries) is homogeneous, ranging between 1.4 and 1.7 (mean = 1.6), and the mean area-weighted olivine aspect ratio does not exceed 2.2 for thin sections showing a well-defined lineation (e.g., Moa30 or Moa31, Fig. 2, Fig. S2).

Opx occurs mostly as large porphyroclasts with an equivalent grain size up to 2.9 mm (e.g., Moa30, Fig. 2). These porphyroclasts have very irregular shapes, sinuous grain boundaries with embayments filled by olivine neoblasts, and no shape-preferred orientation. Opx also occurs as small grains with interstitial shapes and cuspate terminations (e.g., Moa30, Fig. 2b, or Moa4, Moa50, Fig. S2). The small Opx crystals most often form a diffuse layering, which also contains high percentages of olivine neoblasts (cf., Moa13 that has 29% of recrystallization or Moa31 with 18.1% of recrystallization in Fig. S2).

Cpx occurs quasi exclusively as small grains with interstitial cuspate shapes, and rare coarse grains have irregular shape. Cpx is usually much smaller than Opx (Fig. 2, Fig. S2) and rarely occurs as grains >1 mm (Moa10, Moa12 and Moa37, Table S2, Fig. S2). Mean Cpx grain sizes range between 18 and 61 μm (Fig. S2, Table S1 and S2). It occurs either as dispersed or forming trails, often associated with fine-grained Opx and olivine neoblasts (e.g., Moa3, Moa4, and Moa13 in Fig. S2).

While the samples are very fresh at the macroscopic scale, SEM characterization (Fig. 3) permits (1) to confirm the very limited presence of serpentine, essentially along secondary cracks and not along grain boundaries, and (2) to identify very fine Cpx exsolution lamellae in Opx, which indicates (fast) cooling of these peridotites, and (3) minute amounts of pargasite (<0.1%). Despite pervasive fractures, most grain

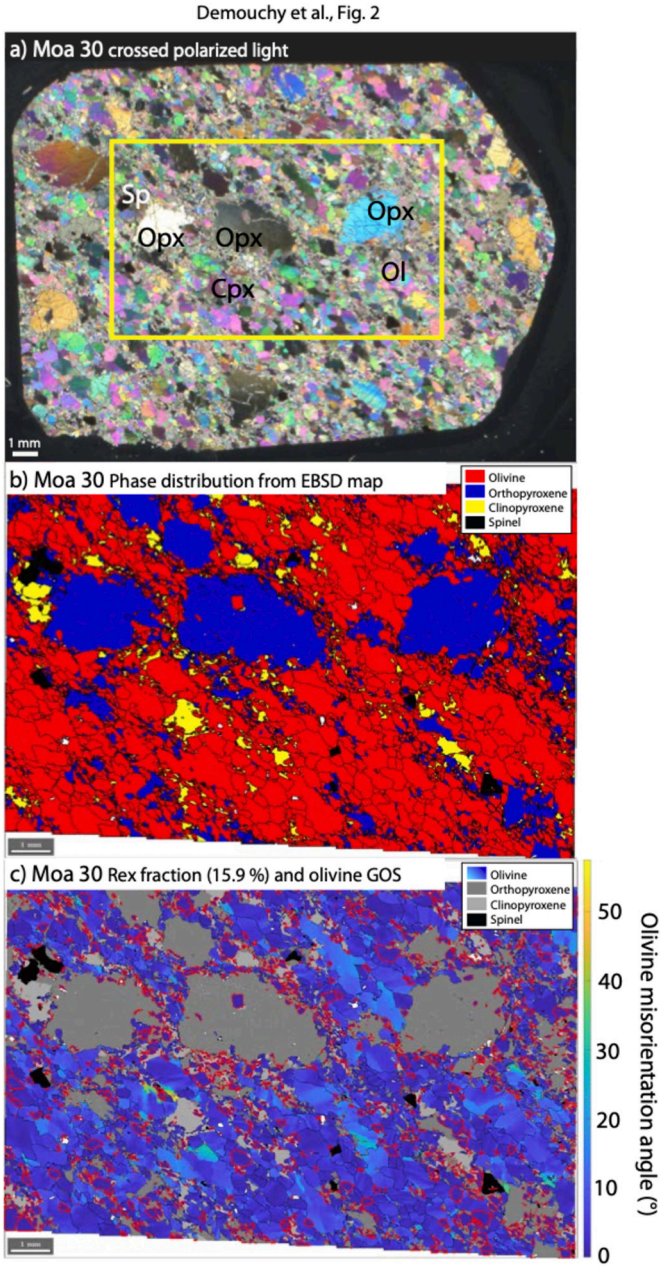

Fig. 2. Microstructure of sample Moa30; **(a)** optical microphotograph in cross polarized light showing typical microstructures and mineralogy of Moa peridotites; **(b)** phase map, for a selected area in yellow in (a), constructed using EBSD data; **(c)** Composite map constructed using EBSD data showing the grain orientation spread (GOS) in olivine (blue gradients) and the recrystallized fraction of olivine, shown with a red grain boundary lining. Orthopyroxenes are displayed in dark gray, clinopyroxenes in light gray, and spinel in black. See main text for details and in the full data set in Fig. S2. (For interpretation of the references to colour in this figure legend, the reader is referred to the web version of this article.)

boundaries remain closed and free of hydrous minerals (Fig. 3a). In HR-SEM, extremely rare veins (~1 μm wide) filled by Opx and Cpx are observed and can be interpreted as fully crystallized remnant melt (Fig. 3e and f). A notable feature of all major minerals in the two samples investigated by SEM is that although the triple junctions are equilibrated (close to 120°) even for cuspate shaped pyroxenes, the boundaries of the olivine neoblast or secondary pyroxenes remain strongly curved (Fig. 3b), indicating that textural equilibrium as seen in equigranular microstructures in Hawaii peridotite xenoliths (e.g., Tommasi et al.,

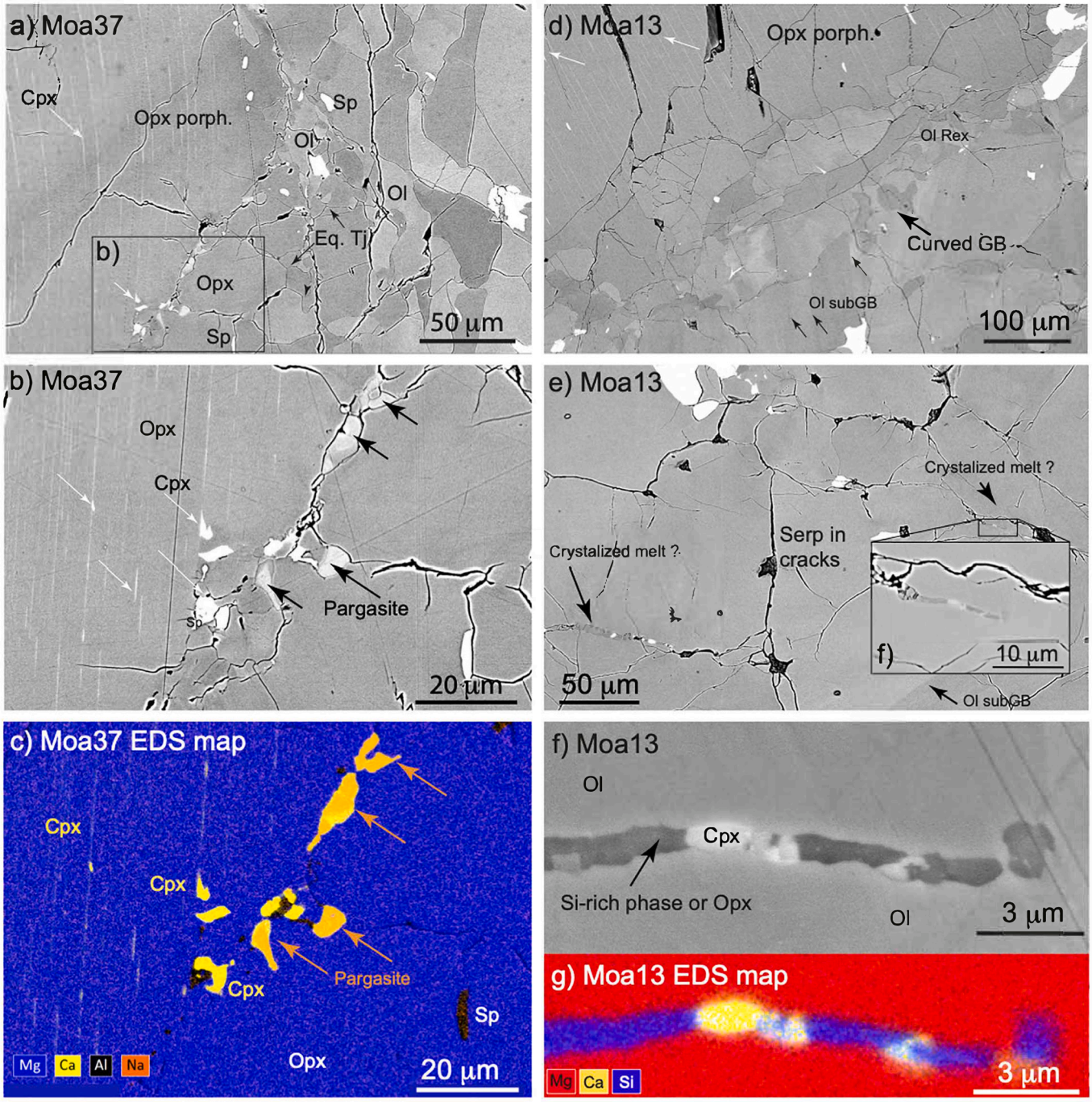

Fig. 3. SEM characterization of small-scale microstructural features not identified by EBSD mapping. Sample Moa 37: **(a)** and **(b)** backscattered electron images showing interstitial pargasite and clinopyroxene lamellae in orthopyroxene porphyroclasts; **(c)** EDS map of **(b)** showing pargasite co-existing closely with cuspate clinopyroxene. Sample Moa 13: **(c), (d)** and **(f)** backscattered electron images showing area with recrystallized olivine, curved grain boundaries, mosaïc of olivine, olivine porphyroclasts with subgrain boundaries, cracks filed with serpentine and narrow fingers filled with a recrystallized orthopyroxene/Si-rich phase. **(f)** HR-SEM image and **(g)** corresponding EDS map, showing veinlet of orthopyroxene inside olivine, where a small clinopyroxene crystalized within the veinlet.

2020) had not been achieved.

3.3. Crystallographic preferred orientation

All studied peridotites display well-developed olivine CPO, with a majority characterized by single maximum concentrations of both [100] and [010] axes of olivine as illustrated for three representative samples with increasing fractions of recrystallized olivine (Moa50, 6.9 Rex %; Moa30, 15.9 Rex %; Moa13, 29 Rex %) in Fig. 4. In this figure, we compare, for the three samples, the bulk olivine CPO to those of the olivine porphyroclasts and recrystallized olivine. In most cases, the olivine pole figures show similar orthorhombic patterns with an axial-[100] tendency, but the recrystallized olivine have more dispersed CPO (Fig. S2).

Olivine CPO for all samples is shown in Fig. S2. The dataset comprises 11 olivine CPOs with axial-[010] (also known as AG-type), defined by a [010] point maximum and girdle distributions of [100] and [001], and 6 orthorhombic (also A-type), characterized by point maxima of [100], [010], and [001]. One sample (Moa24) has an axial-[100] (D-type) defined by a [100] point maximum and girdle

Table 2
Summary of the olivine key microstructural indicators of the studied Moa peridotites obtained from EBSD. Area-weighted mean grain size, J-index, BA-index, and mean misorientation angle relative to the mean grain orientation spread (GOS), apparent aspect ratio, and shape factor for olivine. All these indexes are calculated using one data point per pixel. See Table S2 for the full statistical dataset, notably the numbers of grain plotted in the pole figures.

Olivine	Ol Rex %	Nb grain	Mean grain size*	J-index all	J-index Rex	J-index Porph	BA-index all	BA-index Rex	BA-index Proph	Mean GOS	Mean GOS porph	Shape Factor	Aspect ratio
Moa3	13.2	582	84.3	8.01	4.2	9.8	0.53	0.42	0.56	1.69	4.22	1.7	2.1
Moa4	31.3	1280	54.7	2.90	2.7	4.3	0.64	0.74	0.54	1.17	3.45	1.7	2.2
Moa5	12.9	4935	46.3	4.84	2.5	5.6	0.23	0.20	0.24	1.30	3.87	1.6	1.9
Moa7	9.5	3440	107.1	4.10	2.6	4.4	0.13	0.21	0.12	1.86	4.01	1.6	1.8
Moa10	9.6	3207	93.1	5.45	3.4	5.8	0.19	0.18	0.19	1.90	3.93	1.6	1.8
Moa12	20.3	9268	78.1	2.42	2.0	2.7	0.26	0.25	0.29	1.67	3.80	1.6	1.9
Moa13	29.0	8021	72.2	2.01	1.5	2.5	0.58	0.37	0.65	1.46	3.56	1.6	1.8
Moa16	22.6	6115	79.0	2.22	1.9	2.5	0.14	0.29	0.15	1.59	3.78	1.6	1.9
Moa20	12.6	4757	95.1	3.15	2.9	3.4	0.60	0.41	0.63	1.95	3.74	1.6	1.9
Moa22	10.8	2757	107.8	3.37	2.4	3.7	0.43	0.31	0.44	1.95	3.76	1.6	1.9
Moa24	28.4	4715	95.5	2.58	2.4	3.0	0.76	0.63	0.81	1.56	3.38	1.6	2.0
Moa30	15.9	4342	104.2	2.37	1.9	2.6	0.41	0.51	0.40	1.85	3.56	1.6	2.1
Moa31	18.3	4463	90.7	1.93	1.7	2.2	0.28	0.32	0.36	1.90	3.53	1.6	2.1
Moa34	9.6	4708	66.2	3.59	2.3	3.9	0.26	0.40	0.25	1.87	4.06	1.5	1.8
Moa37	12.6	11,803	69.4	2.67	1.9	2.9	0.17	0.14	0.17	1.65	4.23	1.5	1.8
Moa50	6.9	4271	82.0	4.11	2.1	4.4	0.29	0.30	0.29	1.69	4.23	1.5	1.8
Moa55	17.6	9096	59.1	2.59	1.6	3.0	0.31	0.32	0.34	1.51	3.91	1.4	1.6
Moa56	14.7	6861	72.5	3.01	1.8	3.4	0.25	0.26	0.25	1.58	4.01	1.6	1.8

* We report here the apparent mean grain size, which differs from the true mean diameter of grains defined as d = K1 x L, where K1 is a constant depending on the grain shape equals to 1.5 for equ-dimensional grains and L is the mean interval between two grain boundaries (i.e., equivalent to the mean apparent grain size obtained using EBSD maps), see Etheridge and Wilkie (1981) and Vauchez (1987) for details.

distributions of [010] and [001] (see Table S2 for correspondence of CPO types and slip systems). A finer analysis shows that olivine in several samples have transitional CPO transitional between axial-[010] and orthorhombic (Moa31, Moa50, due to scatter of [001] axes) or transitional between orthorhombic and axial-[100] (Moa4, Moa 13 and Moa20). Such continuum is expected (Demouchy et al., 2023).

We used the J-index and the BA-index (calculated for all olivine grains or solely the porphyroclasts or Rex olivine) to further quantify the variations in intensity and symmetry of the olivine CPO among the studied samples (Table 2, S2, Fig. 5). In all samples, the CPO of the porphyroclastic olivine is more concentrated (higher J-index) than that of the recrystallized olivine. The intensity of the CPO of both populations decreases with the increase of the recrystallized olivine fraction (Fig. 4, Fig. 5a, Table 2). Most samples have a bulk J-index <4, but bulk J-indexes drop from 4.1 (Moa50, 6.9% Rex for the least recrystallized peridotite) down to 2.1 (Moa 13, 29% Rex, for the most recrystallized peridotite). The J-index of the recrystallized olivine fraction (mostly J-index<3) is less sensitive to the intensity of the recrystallization (Table 2). Note that the three samples for which EBSD data is derived from higher resolution maps (3 μm) display relatively higher J-indexes indicating that the CPO intensity is overestimated since the analyzed area is too small to be representative of the entire thin section (local effect).

The BA-index determined for the bulk olivine population ranges from 0.13 to 0.76 (Moa7 and Moa24, respectively). The most recrystallized samples display orthorhombic to fiber–[100] patterns (Fig. 5b), but otherwise there is no well-defined positive correlation between the BA-index and the recrystallized olivine fraction.

The area-weighted mean grain orientation spread of olivine decreases from 1.95° to 1.17° and the area-weighted mean grain size from 108 μm to 46 μm as recrystallization progressed (Fig. 5d). In contrast, recrystallization does not significantly impact the aspect ratio or shape factor (Fig. S3).

Pyroxenes CPOs are plotted with the porphyroclasts displayed as points, overlying that of the recrystallized pyroxene fraction, which are displayed as density contours. Differently to olivine, the recrystallized pyroxene fraction was discriminated based solely on a grain size threshold of 250 μm and 100 μm for orthopyroxenes and clinopyroxenes, respectively. These thresholds are determined based on the grain size distribution for the two phases in the entire dataset. Pyroxenes CPOs are usually more dispersed than the olivine CPOs. Comparison of the neoblast to the porphyroclasts CPOs highlights some inheritance, but also development of new orientations unrelated to that of the pyroxenes porphyroclasts. The values of J-index for Opx range between 2.8 and 16.4 and for Cpx between 3.8 and 25 (see Table S2). The high J-index values are overestimates because the bulk CPO and hence the J-index are dominated by the orientation of a few very coarse porphyroclasts in these samples. In the least recrystallized samples, the Opx CPOs show a weak correlation with the olivine CPOs (Fig. 4), that is alignment of the $[001]_{opx}$ axes maximum at a small angle to the $[100]_{ol}$ axes maximum and of the $[100]_{opx}$ axes to the $[010]_{ol}$ axis of olivine. However, in the most recrystallized peridotites neither Opx CPOs nor Cpx CPOs are correlated to the olivine CPOs.

3.4. Seismic properties

Since all Moa peridotites have similar CPOs and compositions, they have similar seismic properties. Thus, we only report seismic properties (mean seismic velocities and maximum propagation and polarization anisotropies for P- and S-waves) for samples Moa50 (strong fiber-[010] olivine CPO, low degree of recrystallization), Moa30 (moderate CPO in between orthorhombic and fiber-[100] olivine CPO), Moa13 (most recrystallized texture and low J-index), as well as the mean seismic properties of all 18 samples in Table 3. Only the mean seismic properties are shown in Fig. 6. The densities, elastic constant tensors (*Cijkl*) and resulting seismic properties for each sample are compiled in Table S3.

Both the individual samples and their mean show typical upper mantle seismic anisotropy patterns, with fast polarization of S-waves and fast propagation of P-waves parallel to the maximum concentration of olivine [100] axes, which likely marks the flow direction (Fig. 6). The maximum P-wave propagation anisotropy for the mean Moa sample is 7.3% (Table 3). The maximum S-wave polarization anisotropy (5.1%, Table 3) is obtained for waves propagating in the flow plane at ~45° to the flow direction. The maximum propagation anisotropy for the fast S-wave (S1) is of 5.1% and for the slow S-wave (S2) is of 2.5%. S1 waves propagate faster in the flow plane and S2 waves are slowest when propagating normal to the flow direction. The Vp/Vs ratio ranges between 1.69 and 1.75 with the highest values obtained for waves

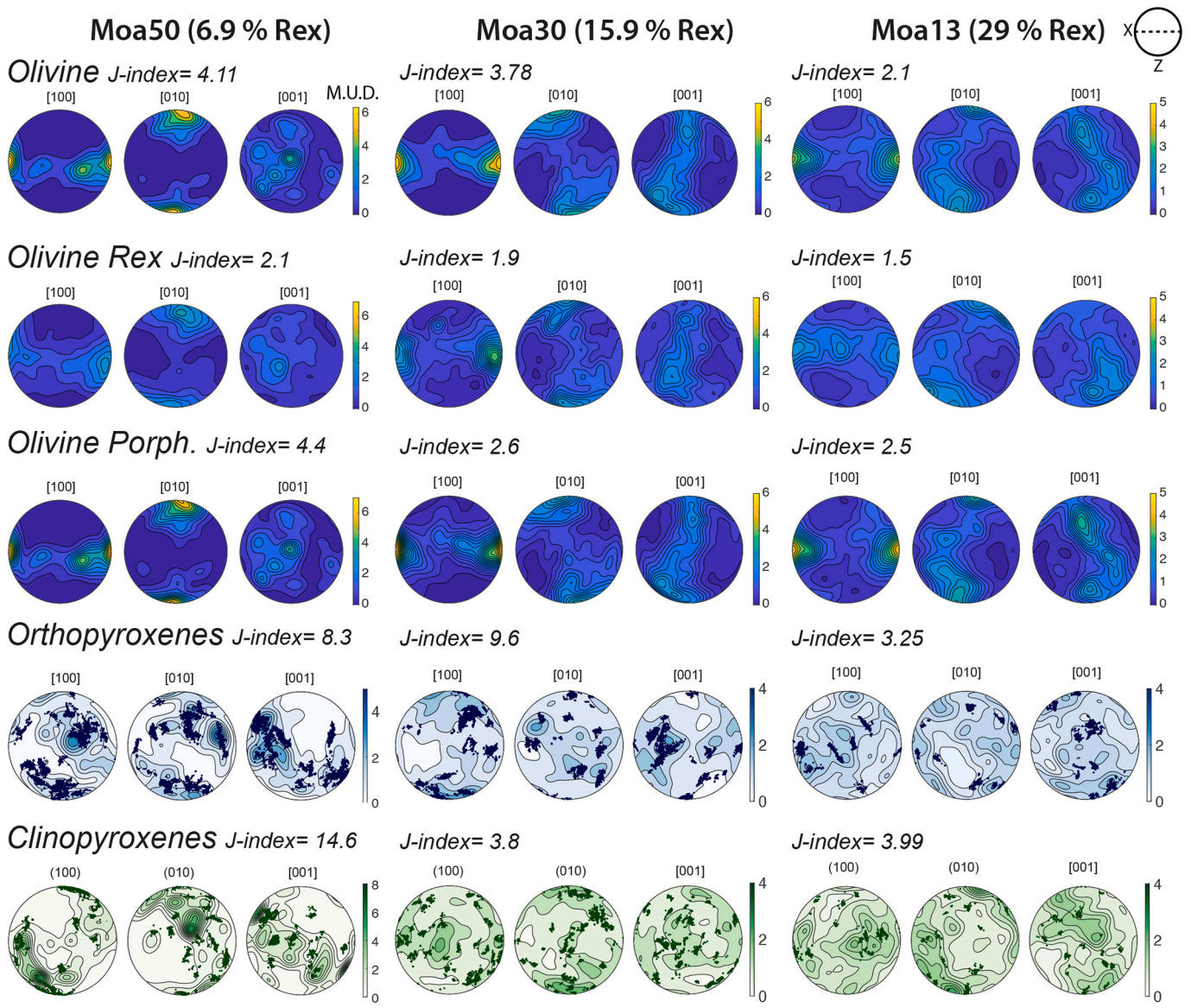

Fig. 4. Pole figures for olivine (all, % Rex = only recrystallized olivine fraction: Porph = only porphyroclastic fraction), orthopyroxene, and clinopyroxene for a selection of three representative samples with increasing amount of recrystallized olivine: Moa50 (6.9% Rex), Moa30 (15.9% Rex) and Moa13 (29% Rex). Equal-area hemisphere stereographic projections. Note that since the lineation and foliation were not well-defined in these samples, CPO are rotated to place the [100] axis maxima of olivine parallel to the x (East-West) direction (see method section for details). Contours are multiples of uniform density. Pole figures of orthopyroxene and clinopyroxene are displayed with porphyroclasts plotted as points overlaying the recrystallized fraction plotted as contours lines. The recrystallized grains of orthopyroxene are grains <250 μm, and a threshold grain size of 100 mm is used for clinopyroxene. NB1: if the orientation distribution of [100] of olivine is correlated with the orientation distribution of [001] of the pyroxenes, the three mineral phases are interpreted as *syn*-deformed. NB2: J-index = 1 is the definition of the perfectly random orientation of the crystals. See main text for details. The numbers of grains for each phase are reported in Table S2.

propagating parallel to the flow direction and the minimum for waves propagating normal to it.

Analysis of the seismic properties of individual samples shows that an increase in the recrystallized olivine fraction results in a decrease in the anisotropy as illustrated by Fig. 7. The maximum P, S1, and S2 propagation and S-wave polarization anisotropies of the most recrystallized sample Moa13 are ca. half of that of the least recrystallized sample Moa50 (Table 3, and S3). As expected, the recrystallization does not affect the mean P- and S-wave velocities, which only depend on the modal composition (density), temperature and pressure conditions (e.g., Tommasi and Vauchez, 2015; Tommasi et al., 2020).

3.5. Infrared spectra and hydrogen concentrations

All 18 peridotite samples were analyzed, but only 10 samples (Moa4, Moa5, Moa7, Moa12, Moa16, Moa20, Moa22, Moa24, Moa30 and Moa 37) yielded FTIR spectra uncontaminated by pervasive hydrous minerals (serpentine and amphibole) even if the samples are all extremely fresh. The hydrogen concentrations determined from these spectra are reported in Table 4. Only one sample (Moa37) had grains clean enough to provide a set of spectra for olivine, orthopyroxene and clinopyroxene as presented in Fig. 8a. In the remaining samples, only coarse orthopyroxene porphyroclasts provided satisfying spectra (Fig. 8b), for which contamination by serpentine or amphibole could be deconvolved. FTIR spectra permitted to identify serpentine, and amphibole as shown in Fig. 8, with the well-known absorption band at 3686 cm^{-1} corresponding to structural OH^- groups in serpentines (Miller et al., 1987; Post and Borer, 2000; Baptiste et al., 2012) and the absorption band at 3670 cm^{-1} OH^- groups matching amphibole lamellae (Skogby, 2006). Determination of the hydrogen concentration in the olivine or pyroxenes

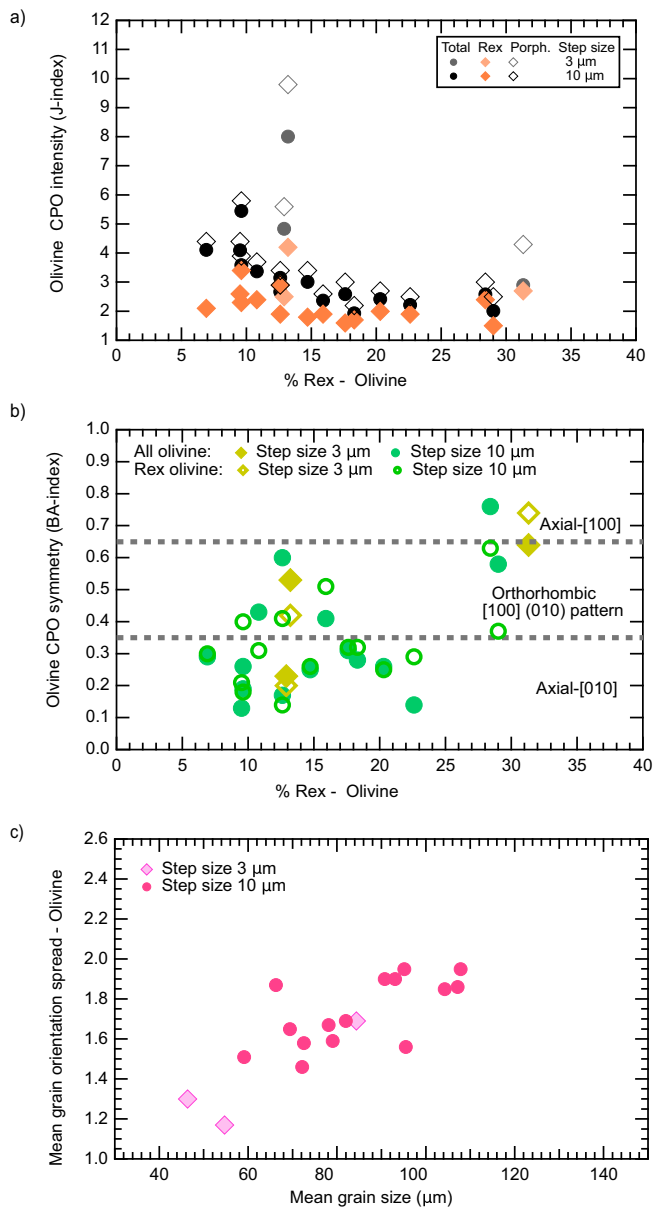

Fig. 5. **(a)** Texture strength (J-index) as a function of the recrystallized olivine fraction (% Rex) in Moa peridotites. A distinction is shown for EBSD maps acquired with a step size of 3 µm or 10 µm; **(b)** texture symmetry (BA-index, all olivine) as a function of % Rex; **(c)** olivine grain orientation spread as a function of the mean grain size of olivine.

neoblasts was not possible in the samples. Despite these difficulties, hydrogen concentration in mantle peridotites exhumed by tectonic processes could be quantified for the first time.

Only two spectra of olivine could be acquired (in sample Moa16 and Moa37, Table S1). The spectra display the hydroxyl bands typical of mantle-derived olivine at 3572, 3525 (Demouchy and Bolfan-Casanova, 2016) but these bands are here very weak as shown in Fig. 8a, and a broad band dominating the spectrum at 3240–3230 cm^{-1}, which is attributed to H decorating Mg-vacancies (e.g., Thoraval et al., 2019). A weak band at ~3417 cm^{-1} is observed, attributed to TiChu lamellae (Thoraval et al., 2019) and the IR bands ~3690 cm^{-1} is typical of serpentine (Post and Borer, 2000). Once the hydrous minerals contributions are excluded (by deconvolution), the hydrogen concentration is estimated to 13–18 wt ppm H_2O.

In the peridotite sample Moa37, several spectra of clinopyroxene could be also acquired. As this mineral is strongly anisotropic (see Fig. 7, Skogby, 2006), acquisitions are performed with different orientations. Two typical spectra are shown on Fig. 8a. The hydroxyl bands are located at 3644, 3520, 3468, 3360 and 3224 cm^{-1}. While the bands at ~3640, 3540, 3460 and 3360 are typical of clinopyroxene in peridotite xenoliths (e.g., Skogby, 2006; Demouchy et al., 2015), the weak broad band at 3224 cm^{-1} is not normally observed in mantle-derived clinopyroxene. This band was excluded during hydrogen quantification, as well as serpentine or amphibole-related bands. The estimated hydrogen concentrations range between 244 and 266 wt ppm H_2O with a mean value of 255 wt ppm H_2O.

As mentioned above, the acquisition of high-quality spectra was a challenge for olivine and clinopyroxene, while porphyroclastic orthopyroxenes were easier to analyze. Representative unpolarized spectra are presented in Fig. 8b. The hydroxyl bands are located at 3596, 3564, 3520, and 3416 cm^{-1}. The same bands are commonly observed in Opx from peridotite xenoliths (e.g., Skogby, 2006; Demouchy et al., 2015). Once hydroxyl bands from serpentine or amphibole contamination are removed, estimated hydrogen concentrations range from 53 to 175 wt ppm H_2O with an mean value of 112 wt ppm H_2O for the 9 set of Moa peridotites. The full set of normalized absorbances and hydrogen concentrations is given in Table S1.

The determination of hydrogen concentrations in the three coexisting NAMs in lherzolite Moa37 permits to estimate a bulk water content of 66 wt ppm H_2O, as well as hydrogen concentration ratios between the different minerals: opx/ol = 7.65 and opx/cpx = 1.86. Assuming that hydrogen concentrations ratio in Moa37 is representative of the partitioning at depth and knowing the mean volume fraction of each phase from EBSD maps (Table 1), the bulk water content in the other Moa peridotites can be calculated using the concentration ratios and the mean hydrogen concentration of the orthopyroxene. Based on hydrogen concentrations of NAMS only, it yields a bulk water content for this set of Moa peridotites of ~50 wt ppm H_2O. If a minute amount of pargasite is considered (volume fraction of 0.1%, theoretically water saturated with 2.0 wt% H_2O), the bulk water content reaches ~70 wt ppm H_2O.

4. Discussion

4.1. Petrogenesis and ductile deformation

Based on previous studies, the Moa peridotites bodies are interpreted as an ophiolite section exhumed tectonically during arc uplift of the overriding Asian plate, possibly helped by the partial break-off of the oceanic section of Australia slab (Fig. 1c, Ishikawa et al., 2007; Kaneko et al., 2007). Ishikawa et al. (2007) reported petrological and geochemical evidence (e.g., from major and trace elements, Cr# in

Table 3
Calculated seismic properties at 900 °C and 1.2 GPa (velocities in $km.s^{-1}$ and anisotropies in %) of samples Moa50, Moa30, Moa13 and mean properties for the 18 spinel-bearing peridotites. The full data set (densities, *Cij* and seismic properties of each sample) is available in Table S3.

Sample	Density	Mean Vp (km/s)	AVp %	Mean Vs (km/s)	AVs1%	AVs2%	Mean AVs %	Max AVsPol	Max Vp/Vs1	Min Vp/Vs1
Moa50	3.32	7.88	9.8	4.51	6.0	4.8	5.4	7.9	1.9	1.7
Moa30	3.31	7.85	6.0	4.52	3.8	3.6	3.7	5.4	1.8	1.7
Moa13	3.31	7.85	4.8	4.52	2.3	2.4	2.4	4.6	1.8	1.7
Mean	3.31	7.86	7.3	4.52	5.1	2.7	3.9	5.9	1.8	1.7

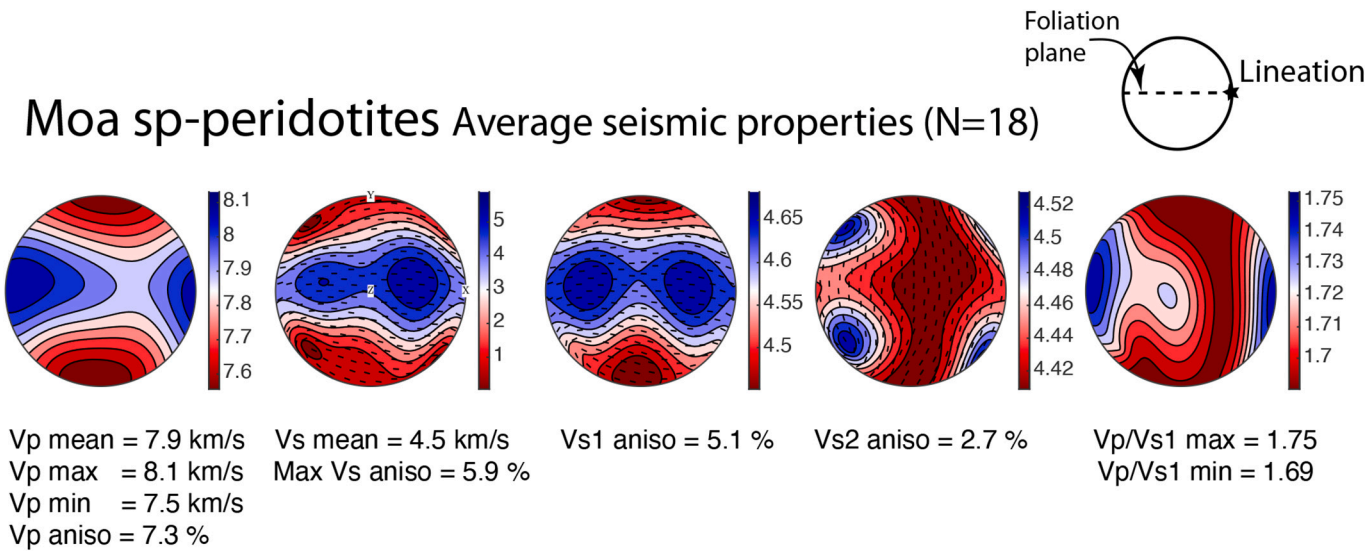

Fig. 6. Mean seismic anisotropy patterns calculated based on the 18 peridotites at 900 °C and 1.2 GPa. From left to right: P-wave velocity (Vp), S-wave polarization anisotropy (AVs) and the orientation of fast S- wave polarization plane, S_1 wave velocities (VS_1), S_2 wave velocities (VS_2), and the Vp/VS_1 ratio. Lower hemisphere stereographic projection. The common deformation reference frame is indicated by the insert on the top right.

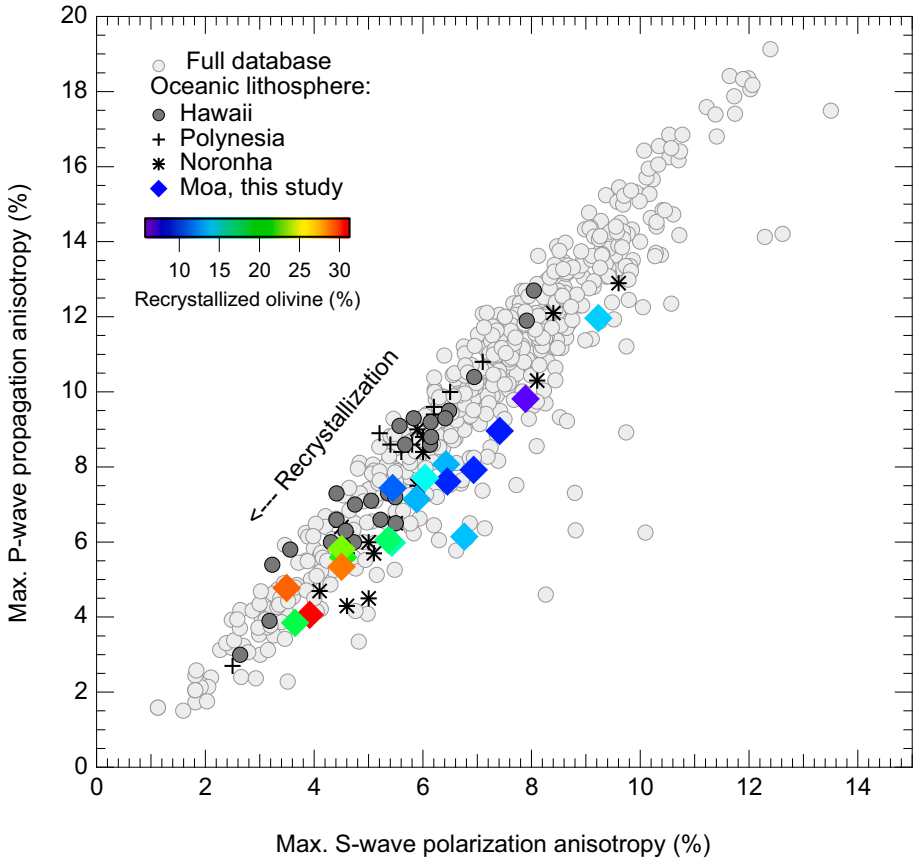

Fig. 7. Maximum anisotropy for Vp and Vs for each peridotite, colour coded based on the % Rex for the Moa Island peridotites. For comparison, we provide a compilation of data for xenoliths from the oceanic mantle lithosphere (for Hawaii, French Polynesia and Fernando de Noronha, from Tommasi et al., 2020), as well as the global seismic anisotropy database from Geosciences Montpellier (from Mainprice et al., 2014, Tommasi and Vauchez, 2015, Demouchy et al., 2023).

spinel, and Al_2O_3 content in orthopyroxenes) that Moa harzburgites are residues of a single but continuous melting, which could represents decompression melting occurring beneath an oceanic ridge. The crystallization of secondary pyroxene observed in the studied harzburgites and lherzolites might be explained by reactive melt percolation or partial crystallization, at the base of the progressively thickening oceanic lithosphere, of melt the fraction not fully extracted at the ridge. Similar modal compositions and microstructures, characterized by quasi absence of primary Cpx, partial dissolution of Opx porphyroclasts, crystallization of cuspate secondary Cpx and Opx, and recrystallization

Table 4
Mean integrated absorption coefficients and corresponding hydrogen concentrations in olivine, orthopyroxene and clinopyroxene. Result for each spectrum is provided in Table S1.

	Thickness	Olivine(1)				Orthopyroxene			Clinopyroxenes		
	(μm)	Nb of sp.	Mean Norm. Abs.	wt ppm H_2O (2)	wt ppm H_2O (3)	Nb of sp.	Mean Norm. Abs.	wt ppm H_2O (4)	Nb of sp.	Mean Norm. Abs.	wt ppm H_2O (4)
Moa3	563	–	*S*(5)		–	–	*S*	–	–	S	–
Moa4	613	–	*S*		–	4	385	74	–	S	–
Moa5	566	–	*S*		–	4	680	131	–	S	–
Moa7	550	–	*S*		–	1	368	71	–	S	–
Moa10	566	–	*S*		–	–	*S*	–	–	S	–
Moa12	593	–	*S*		–	4	781	150	–	S	–
Moa13	544	–	*S*		–	–	*S*	–	–	S	–
Moa16	588	1	37	4	13	–	*S*	–	1	1173	479
Moa20	615	–	*S*		–	4	274	53	–	S	–
Moa22	548	–	*S*		–	2	804	155	–	S	–
Moa24	590	–	*S*		–	3	349	67	–	S	–
Moa30	633	–	*S*		–	2	911	175	–	S	–
Moa31	462	–	*S*		–	–	*S*	–	–	S	–
Moa34	583	–	*S*		–	–	*S*	–	–	S	–
Moa37	595	1	50	6	18	3	709	136	2	602	255
Moa50	596	–	*S*		–	–	*S*	–	–	S	–
Moa55	496	–	*S*		–	–	*S*	–	–	S	–
Moa56	618	–	*S*		–	–	*S*	–	–	S	–

(1): All spectra are obtained with unpolarized Mid-IR light on unoriented grains.
(2): Hydrogen concentration in olivine estimated using the calibration of Paterson (1982) for unpolarized IR on unoriented samples.
(3): Hydrogen concentration in olivine estimated using the calibration of Withers et al. (2012) (C_{OH} = unpolarized Av. Norm. Abs x 3 × 0.119).
(4): Hydrogen concentration in pyroxenes estimated using the calibration of Bell et al. (1995).
(5): Indicate contamination by serpentine which prevented quantification of hydrogen concentrations even if OH detection was qualitatively possible (see main text for details).
NB: for comparison for hydrogen concentration in ppm H/Si or H/ 10^6Si as in Jung and Karato, 2001 or Karato et al., 2008, one needs to apply the following conversion: 1 wt ppm H_2O = 16.35H/10^6Si in Fo_{90}.

of olivine (Fig. 2, Fig. 3b, Fig. S1) were previously reported in ophiolitic peridotites (e.g., Boudier and Nicolas, 1995; Dijkstra et al., 2002; Higgie and Tommasi, 2012; Suhr, 1993).

In the Moa peridotites, the olivine and pyroxene porphyroclasts record an episode of ductile deformation linked to frozen (inherited) texture as oceanic lithosphere formed at a rifting center from the uprising asthenosphere. This initial ductile deformation is evidenced by the grain elongation, subgrain boundary walls, intragranular disorientation of olivine porphyroclasts, undulose extinction and subgrain boundaries in Opx porphyroclasts, the correlation of the olivine CPO to the SPO of the porphyroclasts, and the correlation between the CPO of olivine and Opx (see Fig. 4, parallelism of $[001]_{opx}$ axes to the $[100]_{ol}$ axes, and of $[100]_{opx}$ axes to the $[010]_{ol}$ axes) in the least recrystallized samples. These CPO patterns indicate that ductile deformation is accommodated by dislocation creep with dominant activation of the [100](010) slip system in olivine (e.g., Tommasi and Vauchez, 2015; Demouchy et al., 2023). Here, we propose that the spatial relationship between the recrystallized olivine and the abundance in secondary pyroxenes indicates that the olivine recrystallization might also be a consequence of this reactive melt percolation. Here, the reduced size of neoblast olivine induced by recrystallization can be named static recrystallization, even if it results from olivine dissolution by reactive melt followed by crystallization after melt percolation at small scale (few cm) and not from solid state grain growth during annealing (e.g., Soustelle et al., 2010; Hidas et al., 2016). The ubiquitous cuspate shapes of the secondary pyroxenes imply that the refertilization post-dated the deformation. Decrease of the olivine CPO intensity as a function of increasing recristallization but in static conditions and associated with refertilization is a recurrent feature in oceanic peridotites as illustrated in Fig. 9a (see also Tommasi et al., 2004, 2020). Similar to olivine CPO dispersion resulting from dynamic (*syn*-deformation) recrystallization (e.g. Falus et al., 2011), dispersion of olivine CPO due to melt-rock reactions and static recrystallization is usually, but not systematically, associated with the evolution of the olivine CPO symmetry toward axial-[010] patterns (Fig. 9b).

The re- or neocrystallization of olivine and pyroxenes reduces the seismic anisotropy: the most recrystallized samples have half of the anisotropy of the least recrystallized ones. Similar impact of olivine recrystallization and increased olivine fraction (via decrease of pyroxene fraction) on seismic anisotropy was reported on multiple occasions in both mantle xenoliths and ophiolitic or orogenic peridotite massifs as illustrated by the data compilation reported in Fig. 7 (e.g., Demouchy et al., 2023; Liu et al., 2019; Tommasi et al., 2004, 2020; Tommasi and Vauchez, 2015). However, this variation (Fig. 7) may only be detected by seismic measurements if the refertilization/recrystallization process affected large volumes of the upper mantle.

4.2. *Impact of hydrogen on the rheology of the oceanic mantle lithosphere*

The nominally anhydrous minerals in the Moa peridotites contain small amounts of hydrogen (olivine: 13–18 wt ppm H_2O; orthopyroxene: 58–175 wt ppm H_2O and clinopyroxenes: 244–288 wt ppm H_2O), which yields a bulk water content of 50 wt ppm H_2O based on NAMs for the Moa spinel-bearing peridotites, or 70 wt ppm H_2O if interstitial pargasite is considered. These hydrogen concentrations are the first ones obtained for oceanic (ophiolitic) peridotites. They can be compared to the current hydrogen concentrations in NAMs database, which were essentially built from hydrogen concentrations in NAMs of mantle xenoliths (e.g, Demouchy and Bolfan-Casanova, 2016), and to the data from a single study on a high-pressure garnet-bearing peridotite massif exhumed tectonically (Almklovdalen in Norway, Kim and Jung, 2015), which reported 20–40 wt ppm H_2O in olivine.

For the oceanic mantle lithosphere, a few studies were performed on mantle xenoliths (see Hawaii by Demouchy and Tommasi, 2021; Ontong-Java Plateau (Malaita) by Demouchy et al., 2015; Kamtchatka by Soustelle et al., 2010; Ichinomegata and Okidogo (Japan arc) by Satsukawa et al., 2017) and two on abyssal peridotites (North Atlantic - ODP-Leg 209 by Schmaedicke et al., 2011; Vema fracture zone – Central Atlantic Ocean by Le Roux et al., 2021). The comparison to these data is provided in Fig. 10. Since the pressure and temperature of equilibrium

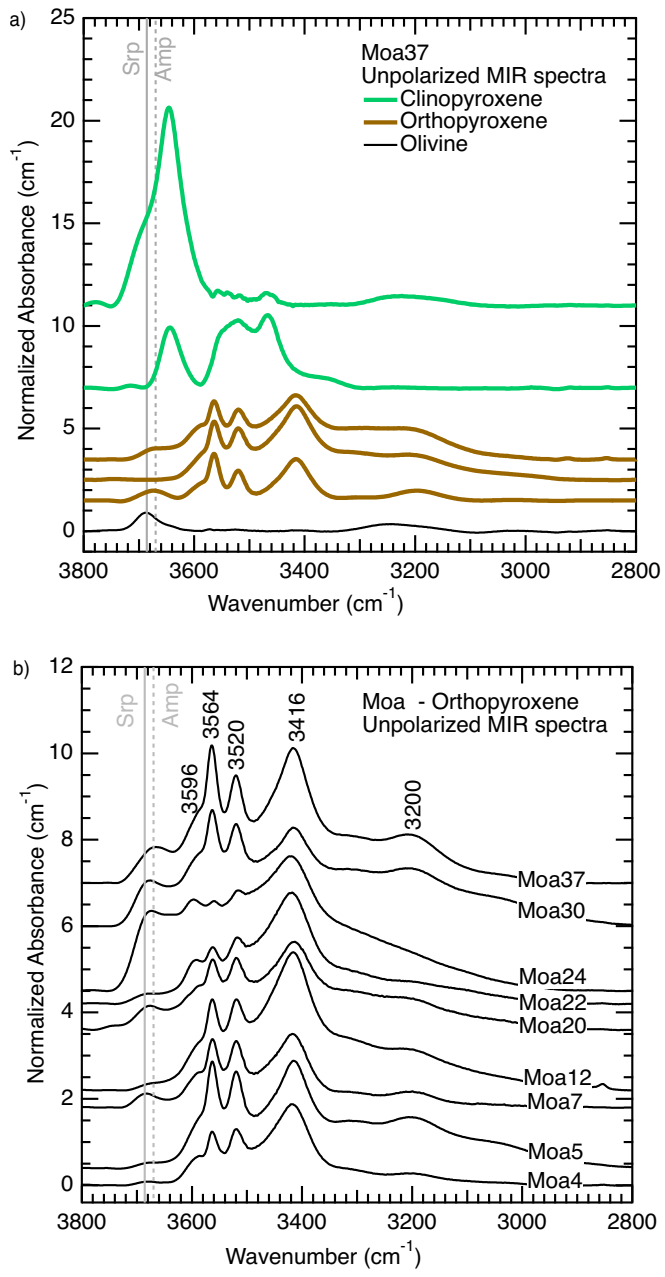

Fig. 8. Representative unpolarized infrared spectra for (a) olivine, orthopyroxenes and clinopyroxenes from lherzolite Moa37 (the least contaminated sample by serpentine). (b) Representative unpolarized infrared spectra for porphyroclastic orthopyroxenes from other Moa peridotites. Spectra are offset vertically for clarity and are all normalized to 1 cm.

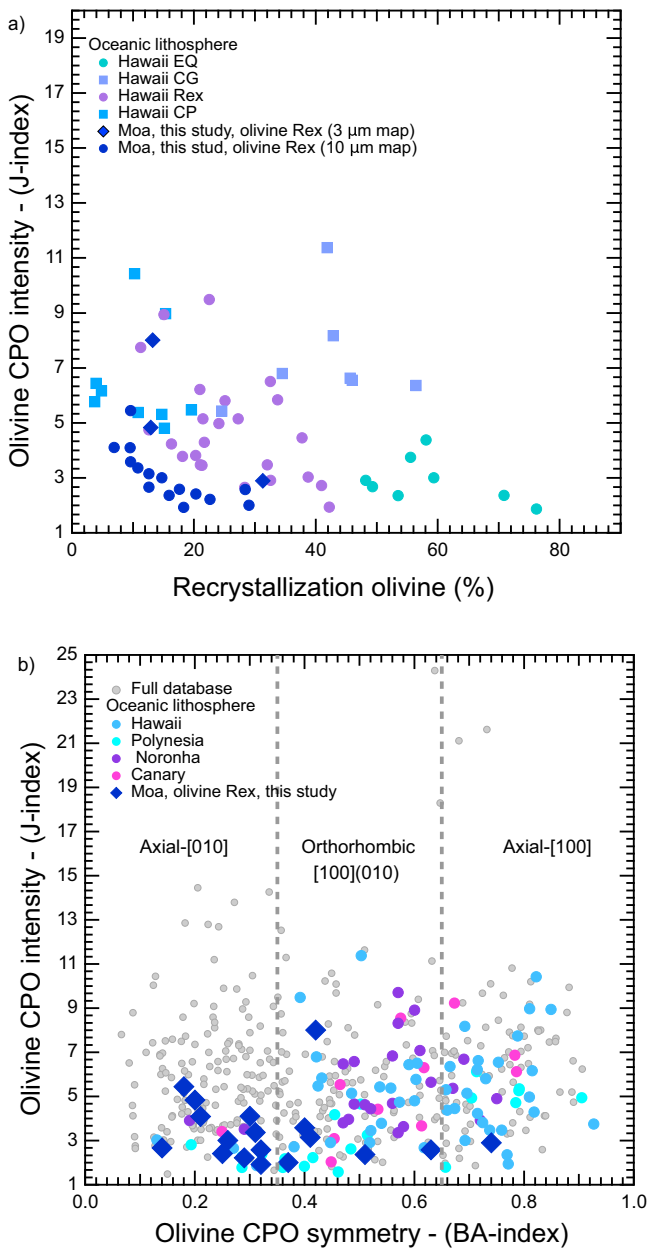

Fig. 9. (a) Compilation of olivine CPO intensity (J-index) as a function of % Rex for the oceanic mantle lithosphere. **(b)** Compilation of olivine CPO intensity (J-index) as a function of olivine CPO symmetry (BA-index, all olivine) for the oceanic lithosphere (see Tommasi et al., 2020 for data source).

are poorly constrained for spinel-bearing peridotites, data are presented per locality and not as a function of depth. We focus here on orthopyroxene hydrogen concentration since it is the phase for which we have the greatest number of reliable measurements (Table 4). Hydrogen concentrations in the Moa Opx (114 wt ppm H_2O) are within the previously observed range of concentration in Opx. Nevertheless, they are slightly lower than the mean value for the oceanic mantle lithosphere (143 wt ppm H_2O based on the data compiled in Fig. 10). Furthermore, there is no drastic difference compared to hydrogen concentrations in Opx from continental mantle lithosphere (see Demouchy and Bolfan-Casanova, 2016; see also Peslier, 2010). The present results confirm that, so far, Opx (and by extension olivine and clinopyroxene) in the oceanic mantle lithosphere are not more hydrated than in the continental mantle lithosphere (cf. Demouchy and Bolfan-Casanova, 2016).

Deformation experiments under hydrous conditions at high pressure, high temperature and varied stresses (e.g., 160–460 MPa, see Jung and Karato, 2001; Jung et al., 2006; Ohuchi and Irifune, 2014) have reported a possible impact of hydrogen on the relative strength of the slip systems accommodating dislocation creep in olivine. Several studies suggested that an hydrogen concentration above ~18 wt ppm H_2O in olivine (using the calibration of Withers et al., 2012; equaling ~9 wt ppm H_2O or ~ 150 ppm H/Si with the calibration of Paterson, 1982) would trigger the activation of [100](001) (E-type, Katayama et al., 2004; Karato et al., 2008) instead of the usual [100](010) slip system (A-Type, Karato et al., 2008). An even higher hydrogen concentration of >86 wt ppm H_2O (with the calibration of Withers et al., 2012, equaling ~43 wt ppm H_2O or ~ 700 ppm H/Si with the calibration of Paterson, 1982) would favor dislocation glide on the [001](100) slip system (C-type, Jung and Karato, 2001; Karato et al., 2008). To date, and despite TEM

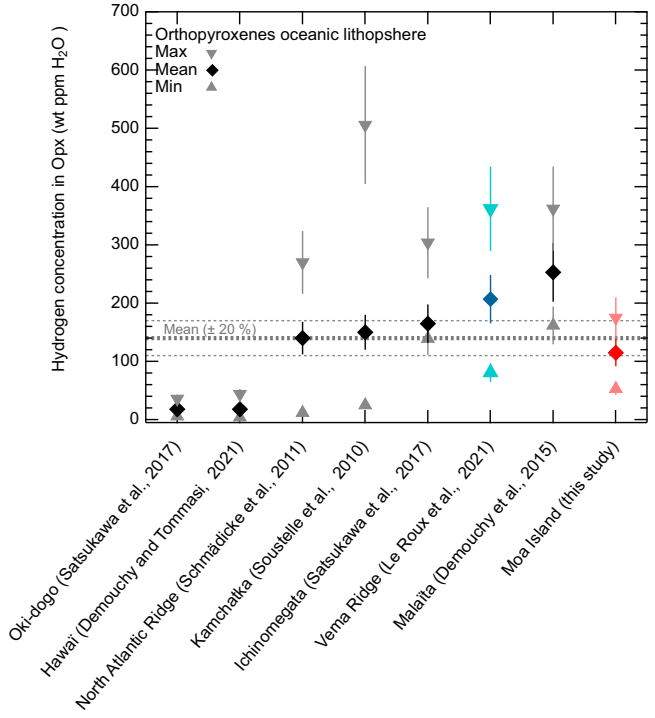

Fig. 10. Compilation of hydrogen concentrations in orthopyroxenes (mostly porphyroblasts) from oceanic mantle lithosphere specimens from this study (red/coral symbols) and from Le Roux et al. (2021); Satsukawa et al. (2017); Schmaedicke et al. (2011); Soustelle et al. (2010); Demouchy et al. (2015), and Demouchy and Tommasi, 2021 Hydrogen concentrations were determined by FTIR except for one study (blue symbols) by Le Roux et al. (2021) who used SIMS. (For interpretation of the references to colour in this figure legend, the reader is referred to the web version of this article.)

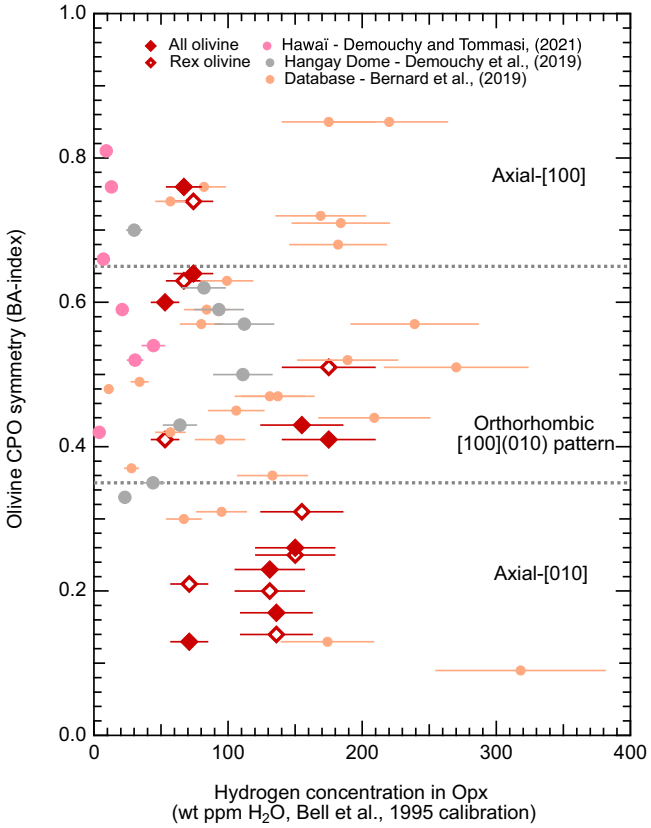

Fig. 11. Compilation of hydrogen concentrations in orthopyroxenes (mostly porphyroblasts) as a function of BA-index for both all olivine and recrystallized olivine (see main text for definition of BA-index, and Table S2) for this study and a large range of mantle lithosphere specimens compiled by Bernard et al. (2019) as well as recent results from Demouchy and Tommasi (2021) and Tommasi et al. (2000) for Hawaii Island (Pali, Oahu Island), as an example of very H-depleted oceanic mantle with high olivine recrystallized fraction and refertilization.

investigations, which show that the different olivine CPOs are related to markedly different dislocation structures, (e.g., Jung et al., 2006), studies on natural samples and numerous experiments at high pressure have not established which are the physical mechanisms at atomic scale that explain how incorporation of H+ in the olivine lattice changes the dislocation dynamics. Furthermore, high-quality FTIR results from naturally deformed olivine from spinel peridotites did not confirm these experiments yet (e.g., Bernard et al., 2019, their Fig. 7; Demouchy and Tommasi, 2021; Demouchy et al., 2019; Tommasi and Vauchez, 2015; Tommasi et al., 2020; Wen et al., 2023). Olivine CPO pointing to dominant [001] glide is mostly described in high-pressure garnet-bearing peridotites associated with eclogites, such as Alpe Arami and Cima de Gagnone in the Alps or Almklovdalen in Norway (Kim and Jung, 2015). The hydrogen concentration in olivine in the Moa peridotites (~13–18 wt ppm H_2O, equivalent to 100–150 ppm H/Si with the calibration of Paterson, 1982 used by Jung and Karato, 2001 and Jung et al., 2006) is just below the limit of the possible transition of slip systems toward dominant activation of the [100](001) slip system. Thus, one should not expect a strong change in olivine CPOs with increasing deformation and recrystallization. Equal activity of the [100](010) and [100](001) slip systems may produce axial-[100] olivine CPO. However, axial-[100] are infrequent among the studied Moa peridotites (Fig. S2). Compilation of a larger dataset from natural samples in Fig. 11 further illustrates the lack of any systematic relationship between hydrogen concentration in Opx and BA-index in olivine.

The interstitial presence of pargasite in very small quantity (volume fraction of pargasite <0.1%) indicates that the percolating melt did contain some water, which led to very minor modal metasomatism (<0.1%). However, we failed to measure hydrogen concentration in the neoformed olivine and pyroxenes, and only obtained data in Opx porphyroclasts and two olivine porphyroclasts. Consequently, we cannot estimate if melt percolation/refertilization produced hydrogen-enrichment or hydrogen depletion in NAMs (expected from pargasite crystallization, Denis et al., 2015).

5. Conclusion

We report petrophysical analyses of 18 mantle specimens from a peridotite massif located on Moa Island (non-volcanic arc of Timor-Tanimbar region). These results permit to infer that these peridotites have undergone (1) ductile deformation (high temperature, low stress), leading to olivine CPOs with fiber-[010] texture and orthorhombic pattern, consistent with the dominant activation of the [100](010) slip system in olivine as in 85% of mantle lithosphere specimens (e.g., Tommasi et al., 2000; Demouchy et al., 2023), and (2) a first event of reactive (continuous) melt percolation, which strongly decreased the primary Cpx fraction, followed by crystallization of secondary pyroxenes, and static recrystallization of olivine (recrystallized olivine fractions range between 7 and 30%). The hydrogen concentrations were quantified in NAMs using FTIR and we have used coarse orthopyroxene as a proxy of the bulk water content. Olivine contains 13–18 ppm H_2O wt; orthopyroxenes 58–175 wt ppm H_2O and clinopyroxenes 244–288 wt ppm H_2O, which yields a bulk water content of 50 wt ppm H_2O for the Moa peridotites (or ~ 70 wt ppm H_2O if the minute amount of pargasite is included). These hydrogen concentrations are the first obtained from a fresh sliver of the oceanic mantle lithosphere exhumed tectonically and not from mantle xenoliths. These hydrogen concentrations agree with

previous mean estimates for the oceanic mantle lithosphere. We further characterize the peridotite samples by estimating the impact of CPO, mineral fractions and olivine recrystallization on seismic properties. The calculation yields typical estimates of seismic wave velocities (mean *Vp* and mean Vs) and anisotropy %, for oceanic mantle lithosphere with only a moderate decrease in seismic anisotropy with increase of the recrystallized fraction of olivine.

CRediT authorship contribution statement

Sylvie Demouchy: Writing – review & editing, Writing – original draft, Validation, Resources, Project administration, Methodology, Investigation, Funding acquisition, Formal analysis, Data curation, Conceptualization. **Fabrice Barou:** Writing – review & editing, Methodology, Formal analysis. **Akira Ishikawa:** Writing – review & editing, Resources. **Emmanuel Gardés:** Writing – review & editing, Resources, Methodology, Investigation, Formal analysis. **Andréa Tommasi:** Writing – review & editing, Software, Methodology, Formal analysis.

Declaration of competing interest

The authors declare the following financial interests/personal relationships which may be considered as potential competing interests:

Sylvie Demouchy reports financial support was provided by CNRS Languedoc-Roussillon Delegation.

Sylvie Demouchy reports financial support was provided by CNRS Auvergne-Rhône-Alpes Delegation.

Sylvie Demouchy reports financial support was provided by University Clermont Auvergne via its Centre International de Recherche Catastrophes Naturelles et Développement Durable (CIR4) program.

Sylvie Demouchy reports financial support was provided by ANR project H-Deep-ISO.

Andréa Tommasi reports financial support was provided by European Research Council.

Data availability

The raw FTIR data are available upon request from the corresponding author, treated FTIR spectra are available at the Zenodo OpenAIRE repository at https://zenodo.org/doi/10.5281/zenodo.10835768. EBSD data used to generate the phase maps and grain orientation maps presented in supplementary material S2 are available at the Zenodo OpenAIRE repository at https://zenodo.org/doi/10.5281/zenodo.10835812.

Acknowledgements

C. Nevado and D. Delmas are thank for providing high-quality sections for FTIR and EBSD. The EBSD-SEM national facility at Geoscience Montpellier and SEM-FIB-STEM CarMa facility are both supported by the Institut National de Sciences de l'Univers (INSU) du Centre National de la Recherche Scientifique (CNRS, France). We acknowledge funding from ANR H-Deep-ISO to S. Demouch; University Clermont Auvergne via its Centre International de Recherche Catastrophes Naturelles et Développement Durable (CIR4) program (MOA project) to S. Demouchy; and the European Research Council (ERC) under the European Union's Horizon 2020 research and innovation program under grant agreement N° 882450 - RhEOVOLUTION to A. Tommasi. This is CIR4-ClerVolc publication N°656.

Appendix A. Supplementary data

Supplementary data to this article can be found online at https://doi.org/10.1016/j.tecto.2024.230443.

References

Abramson, E.H., Brown, J.M., Slutsky, L.J., Zaug, J.M., 1997. The elastic constants of San Carlos olivine to 17 GPa. J. Geophys. Res. Solid Earth 102 (B6), 12253–1226.

Bachmann, F., Hielscher, R., Schaeben, H., 2010. Texture analysis with MTEX – Free and open source software toolbox. Solid State Phenom. 160, 63–68.

Baptiste, V., Tommasi, A., Demouchy, S., 2012. Deformation and hydration of the lithospheric mantle beneath the Kaapval craton. Lithos, Sp. Issue 'Formation, reactivation and destruction of cratons' 149, 31–50. https://doi.org/10.1016/j.lithos.2012.05.001.

Bell, D.R., Ihinger, P.D., Rossman, G.R., 1995. Quantitative and analysis of trace OH in garnet and pyroxenes. Am. Mineral. 80, 465–474.

Bell, D.R., Rossman, G.R., Maldener, J., Endisch, D., Rauch, F., 2003. Hydroxide in olivine: a quantitative determination of the absolute amount and calibration of the IR spectrum. J. Geophys. Res. Solid Earth 108 (B12), 2105. https://doi.org/10.1029/2001JB000679.

Bernard, R.E., Behr, W.M., Becker, T.W., Young, D.J., 2019. Relationships between olivine CPO and deformation parameters in naturally deformed rocks and implications for mantle seismic anisotropy. Geochem. Geophys. Geosyst. 20, 3469–3494. https://doi.org/10.1029/2019GC008289.

Bodinier, J.-L., Godard, M., 2014. Orogenic, Ophiolitic, and Abyssal Peridotites. In: Holland, H.D., Turekian, K.K. (Eds.), Treatise on Geochemistry, , Second editionvol. 3. Elsevier, Oxford, pp. 103–167.

Boudier, F., Nicolas, A., 1995. Nature of the Moho transition zone in the Oman ophiolite. J. Petrol. 36 (3), 777–796.

Brey, G.P., Köhler, T., 1990. Geothermobarometry in four-phase lherzolite II. New thermobarometers, and practical assessment of existing thermobarometers. J. Petrol. 31, 1353–1378.

Bunge, H.-J., 1982. In: Texture Analysis in Materials Science. Butterworths, London, p. 593.

Chai, M., Brown, J.M., Slutsky, L.J., 1997a. The elastic constants of an aluminous orthopyroxene to 12.5 GPa. J. Geophys. Res. Solid Earth 102 (B7), 14779–14785.

Chai, M., Brown, J.M., Slutsky, L.J., 1997b. The elastic constants of a pyrope-grossular-almandine garnet to 20 GPa. Geophys. Res. Lett. 24 (5), 523–526.

Courdurier-Curveur, A., Singh, S.C., Deighton, I., 2021. Timor Collision Front Segmentation Reveals Potentials for Great Earthquakes in the Western Outer Banda Arc. Frontiers Earth Sci, Eastern Indonesia. https://doi.org/10.3389/feart.2021.640928.

Demouchy, S., Alard, O., 2021. Hydrogen, minor, trace and ultra-trace elements distribution in natural olivines. Contrib. Mineral. Petrol. 176, 26. https://doi.org/10.1007/s00410-021-01778-5.

Demouchy, S., Bolfan-Casanova, N., 2016. Distribution and transport of hydrogen in the lithospheric mantle: a review. Lithos 240–243, 402–425. https://doi.org/10.1016/j.lithos.2015.11.012.

Demouchy, S., Tommasi, A., 2021. From dry to damp and stiff mantle lithosphere by reactive melt percolation atop the Hawaii plume. Earth Planet. Sci. Lett. 574, 117159 https://doi.org/10.1016/j.epsl.2021.117159.

Demouchy, S., Ishikawa, A., Tommasi, A., Alard, O., Keshav, S., 2015. Characterisation of the hydration in the oceanic mantle lithosphere: peridotite xenoliths from Ontong Java Plateau as an example. Lithos 212-215, 189–201. https://doi.org/10.1016/j.lithos.2014.11.005.

Demouchy, S., Tommasi, A., Ionov, D., Higgie, K., Carlson, R.W., 2019. Microstructures, Water Contents, and Seismic Properties of the Mantle Lithosphere beneath the Northern Limit of the Hangay Dome. Geochem. Geophys. Geosyst, Mongolia. https://doi.org/10.1029/2018GC007931.

Demouchy, S., Wang, Q., Tommasi, A., 2023. Driving Upper Mantle Flow - Olivine Mechanical Properties and Anisotropy. Elements 19, 151–157. https://doi.org/10.2138/gselements.19.3.151.

Denis, C.M.M., Alard, O., Demouchy, S., 2015. Water content and hydrogen behavior during metasomatism in the uppermost mantle beneath Ray Pic volcano (Massif Central, France). Lithos 237-237, 256–274. https://doi.org/10.1016/j.lithos.2015.08.013.

Dijkstra, A.H., Drury, M.R., Frijhoff, R.M., 2002. Microstructures and lattice fabrics in the Hilti mantle section (Oman Ophiolite): evidence for shear localization and melt weakening in the crust–mantle transition zone? J. Geophys. Res. Solid Earth 107 (B11), 2–18.

Etheridge, M.A., Wilkie, J.C., 1981. An assessment of dynamically recrystallized grain size as a paleopiezometer in quartz-bearing mylonite zone. Tectonophysics 78, 475–508.

Falus, G., Tommasi, A., Soustelle, V., 2011. The effect of dynamic recrystallization on olivine crystal preferred orientations in mantles xenoliths deformed under varied stress conditions. J. Struct. Geol. 33, 1528–1540.

Férot, A., Bolfan-Casanova, N., 2012. Water storage capacity in olivine and pyroxene to 14 GPa: Implications for the water content of the Earth's upper mantle and nature of seismic discontinuities. Earth Planet. Sci. Lett. 349-350, 218–230.

Hidas, K., Tommasi, A., Garrido, C.J., Padron-Navarta, J.-A., Mainprice, D., Vauchez, A., Barou, F., Marchesi, C., 2016. Fluid-assisted strain localization in the shallow subcontinental lithospheric mantle. Lithos 262, 636–650.

Hielscher, R., Schaeben, H., 2008. A novel pole figure inversion method: specification of the MTEX algorithm. J. Appl. Crystallogr. 41, 1024–1037.

Higgie, K., Tommasi, A., 2012. Deformation of a partially molten mantle: Constraints from plagioclase-lherzolites from Lanzo, western Alps. Tectonophysics 615-616. https://doi.org/10.1016/j.tecto.2014.01.007, 167–18.

Ishikawa, A., Kaneko, Y., Kadarusman, A., Ota, T., 2007. Multiple generations of forearc mafic-ultramafic rocks in the Timor-Tanimbar ophiolite, Eastern Indonesia. Gondwana Res. 11 (1–2), 200–217.

Ishikawa, A., Nakamura, N., Yokoyama, T., 2021. Highly siderophile element mobility during serpentinization of mantle wedge peridotite. Goldschmidt Conf. https://doi.org/10.7185/gold2021.7449, 2021, Abs.
Jung, H., Karato, S.-I., 2001. Water-induced fabric transitions in olivine. Science 293, 1460–1463.
Jung, H., Katayama, I., Jiang, Z., Hiraga, T., Karato, S., 2006. Effect of water and stress on the lattice preferred orientation (LPO) of olivine. Tectonophysics 421, 1–22.
Jung, H., Lee, J., Ko, B., Jung, S., Park, M., Cao, Y., Song, S., 2013. Natural Type-C olivine fabrics in garnet peridotites in North Qaidam UHP collision belt, NW China. Tectonophysics 594, 91–102.
Jung, S., Jung, H., Austrheim, H., 2014. Characterization of olivine fabrics and mylonite in the presence of fluid and implications for seismic anisotropy and shear localization. Earth Planets Space 66, 41–21.
Kadarusman, A., Maruyama, S., Kaneko, Y., Ota, T., Ishikawa, A., Sopaheluwakan, J., Omori, S., 2010. World's youngest blueschist belt from Leti Island in the non-volcanic Banda outer arc of Eastern Indonesia. Gondwana Res. 18, 189–204.
Kaneko, Y., Maryalana, S., Kaderusman, A., Ota, T., Ishikawa, M., Tsujomori, T., Ishikawa, A., Okamoto, K., 2007. On-going orogeny in the outer-arc of the Timor-Tanimbar region, Eastern Indonesia. Gondwana Res. 11 (1–2), 218–233.
Karato, S.I., Jung, H., Katayama, I., Skemer, P., 2008. Geodynamic significance of Seismic Anisotropy of the Upper Mantle: New Insights from Laboratory Studies. Annu. Rev. Earth Planet. Sci. 36, 59–95.
Katayama, I., Jung, H., Karato, S.I., 2004. New type of olivine fabric from deformation experiments at modest water content and low stress. Geology 32, 1045–1048.
Kim, D., Jung, H., 2015. Deformation microstructures of olivine and chlorite in chlorite peridotites from Almklovdalen in the Western Gneiss Region, Southwest Norway, and implications for seismic anisotropy. Int. Geol. Rev. 57, 650–668.
Kovàcs, I., Green, H.W., Rosenthal, A., Hermann, J., O'Neill, H.S.C., Hibberson, W.O., Udvardi, B., 2012. An experimental study of water in nominally anhydrous minerals in the upper mantle near water-saturated solidus. J. Petrol. 53, 2067–2093.
Le Roux, V., Bodinier, J.L., Tommasi, A., Alard, O., Dautria, J.M., Vauchez, A., Riches, A. J.V., 2007. The Lherz spinel lherzolite: Refertilized rather than pristine mantle. Earth Planet. Sci. Lett. 259 (3–4), 599–612.
Le Roux, V., Urann, B.M., Brunelli, D., Bonatti, E., Cipriani, A., Demouchy, S., Monteleone, B.D., 2021. Post-melting hydrogen enrichment in the oceanic lithosphere. Sci. Adv. 7, eabf6071. https://doi.org/10.1126/sciadv.abf6071.
Lin, Y.-C., Chung, S.-L., Maruyama, S., Kadarusman, A., Lee, H.-Y., 2023. The ephemeral history of Earth's youngest supra-subduction zone type ophiolite from Timor. Comm. Earth Environ. 4, 308. https://doi.org/10.1038/s43247-023-00973-5.
Liu, S., Tommasi, A., Vauchez, A., Mazzucchelli, M., 2019. Deformation, annealing, melt-rock interaction, and seismic properties of an old domain of the equatorial Atlantic lithospheric mantle. Tectonics 38, 1029/2018TC005373.
Lopez-Sanchez, M.A., Tommasi, A., Ben Ismail, W., Barou, F., 2021. Dynamic recrystallization by subgrain rotation in olivine revealed by electron backscatter diffraction. Tectonophysics 815. https://doi.org/10.1016/j.tecto.2021.228916.
Mainprice, D., 1990. A fortran program to calculate seismic anisotropy from the lattice preferred orientation of minerals. Comput. Geosci. 16, 385–393.
Mainprice, D., Bachmann, F., Hielscher, R., Schaeben, H., 2014. Descriptive tools for the analysis of texture projects with large datasets using MTEX: Strength, symmetry, and components. In: Faulkner, D.R., Mariani, E., Mecklenburgh, J. (Eds.), Rock Deformation from Field, Experiments and Theory: A Volume in Honour of Ernie Rutter. Geological Society, London. https://doi.org/10.1144/SP409.8. Special Publications, 409.
Miller, G.H., Rossman, G.R., Harlow, G.E., 1987. The natural occurrence of hydroxide in olivine. Phys. Chem. Miner. 14, 461–472.
Ohuchi, T., Irifune, T., 2014. Crystallographic preferred orientation of olivine in the Earth's deep upper mantle. Phys. Earth Planet. Inter. 228, 220–231.
Park, M., Jung, H., 2017. Microstructural evolution of the Yugu peridotites in the Gyeonggi massif, Korea: Implications for olivine fabric transition in mantle shear zones. Tectonophysics 709, 55–68.
Paterson, M.S., 1982. The determination of hydroxyl by infrared absorption in quartz, silicate glasses and similar materials. Bull. Mineral. 105, 20–29.
Peslier, A.H., 2010. A review of water contents of nominally anhydrous minerals in the mantles of Earth, Mars and the Moon. J. Volcanol. Geotherm. Res. 197, 239–258.
Peslier, A.H., Bizimis, M., Matney, M., 2015. Water disequilibrium in olivines from Hawaiian peridotites: recent metasomatism, H diffusion and magma ascent rates. Geochim. Cosmochim. Acta 154, 98–117.
Post, J.L., Borer, L., 2000. High-resolution infrared spectra, physical properties, and micromorphology of serpentines. Appl. Clay Sci. 16, 73–85.
Putirka, K., 2008. Thermometers and Barometers for Volcanic Systems. In: Putirka, K., Tepley, F. (Eds.), Minerals, Inclusions and Volcanic Processes, Reviews in Mineralogy and Geochemistry, Mineralogical Soc. Am., 69, pp. 61–120.
Sang, L., Bass, J.D., 2014. Single-crystal elasticity of diopside to 14 GPa by Brillouin scattering. Phys. Earth Planet. Inter. 228, 75–79.
Satsukawa, T., Godard, M., Demouchy, S., Michibayashi, K., Ildefonse, B., 2017. Chemical interactions in the subduction factory: New insights from an in situ trace elements and hydrogen study of the Ichinomegata and Oki-Dogo mantle xenoliths (Japan). Geochim. Cosmochim. Acta 208, 234–267. https://doi.org/10.1016/j.gca.2017.03.042.
Schmaedicke, E., Gose, J., Will, T.M., 2011. Heterogeneous mantle underneath the North Atlantic: evidence from water in orthopyroxene, mineral composition and equilibrium conditions of spinel peridotite from different locations at the Mid-Atlantic Ridge. Lithos 125, 308–320.
Skemer, P., Warren, J.M., Hansen, L.N., Hirth, G., Kelemen, P.B., 2013. The influence of water and LPO on the initiation and evolution of mantle shear zones. Earth Planet. Sci. Lett. 375, 222–233.
Skogby, H., 2006. Water in natural mantle minerals I: Pyroxenes. In: Water in Nominally Anhydrous Minerals. American Mineralogical Society Geochemical Society, Chantilly (Vir.), pp. 155–167.
Soustelle, V., Tommasi, A., Demouchy, S., Ionov, D., 2010. Deformation and fluid-rock interactions in supra-subduction mantle: Microstructures and water contents in peridotite xenoliths from the Avacha volcano, Kamchatka. J. Petrol. 51, 363–394.
Suhr, G., 1993. Evaluation of upper mantle microstructures in the Table Mountain massif (Bay of Islands ophiolite). J. Struct. Geol. 15 (11), 1273–1292.
Thoraval, C., Demouchy, S., Padron-Navarta, J.-A., 2019. Relative diffusivities of hydrous defects from partially dehydrated natural olivine. Phys. Chem. Miner. 46, 1–13. https://doi.org/10.1007/s00269-018-0982-x.
Tommasi, A., Vauchez, A., 2015. Heterogeneity and anisotropy in the lithospheric mantle. Tectonophysics 661, 11–37.
Tommasi, A., Mainprice, D., Canova, G., Chastel, Y., 2000. Viscoplastic self-consistent and equilibrium-based modeling of olivine lattice preferred orientations. Implications for the upper mantle seismic anisotropy. J. Geophys. Res. 105 (B4), 7893–7908.
Tommasi, A., Godard, M., Coromina, G., Dautria, J.M., Barsczus, H., 2004. Seismic anisotropy and compositionally-induced velocity anomalies in the lithosphere above mantle plumes: a petrological and microstructural study of mantle xenoliths from French Polynesia. Earth Planet. Sci. Lett. 227, 539–556.
Tommasi, A., Mameri, L., Godard, M., 2020. Textural and compositional changes in the lithospheric mantle atop the Hawaiian plume: Consequences for seismic properties. Geochem. Geophys. Geosyst. 21, 19–29. https://doi.org/10.1029/2020GC009138.
Vauchez, A., 1987. The development of discrete shear-zones in granite: stress, strain and changes in deformation mechanisms. Tectonophysics 133, 137–156.
Wen, D.-P., Wang, Y.-F., Zhang, J.-F., 2023. Influence of melt-peridotite interactions on deformation and seismic properties of the upper mantle beneath a destroyed craton: a case study of the Damaping peridotites from the North China Craton. J. Geophys. Res. Solid Earth 128 e2022JB026263.
Withers, A.C., Bureau, H., Raepsaet, C., Hirschmann, M.M., 2012. Calibration of infrared spectroscopy by elastic recoil detection analysis of H in synthetic olivine. Chem. Geol. 334, 92–98.